

FINDING THE FIRST COSMIC EXPLOSIONS. I. PAIR-INSTABILITY SUPERNOVAE

DANIEL J. WHALEN^{1,2}, WESLEY EVEN³, LUCILLE H. FREY^{4,5}, JOSEPH SMIDT¹, JARRETT L. JOHNSON⁶,
 C. C. LOVEKIN¹, CHRIS L. FRYER³, MASSIMO STIAVELLI⁷, DANIEL E. HOLZ⁸, ALEXANDER HEGER⁹,

S. E. WOOSLEY¹⁰, AND AIMEE L. HUNGERFORD⁶

¹ T-2, Los Alamos National Laboratory, Los Alamos, NM 87545, USA

² Universität Heidelberg, Zentrum für Astronomie, Institut für Theoretische Astrophysik, Albert-Ueberle-Str. 2, D-69120 Heidelberg, Germany

³ CCS-2, Los Alamos National Laboratory, Los Alamos, NM 87545, USA

⁴ HPC-3, Los Alamos National Laboratory, Los Alamos, NM 87545, USA

⁵ Department of Computer Science, University of New Mexico, Albuquerque, NM 87131, USA

⁶ XTD-6, Los Alamos National Laboratory, Los Alamos, NM 87545, USA

⁷ Space Telescope Science Institute, 3700 San Martin Drive, Baltimore, MD 21218, USA

⁸ Enrico Fermi Institute, Department of Physics, and Kavli Institute for Cosmological Physics, University of Chicago, Chicago, IL 60637, USA

⁹ Monash Centre for Astrophysics, Monash University, Victoria 3800, Australia

¹⁰ Department of Astronomy and Astrophysics, UCSC, Santa Cruz, CA 95064, USA

Received 2012 November 21; accepted 2013 September 6; published 2013 October 18

ABSTRACT

The first stars are the key to the formation of primitive galaxies, early cosmological reionization and chemical enrichment, and the origin of supermassive black holes. Unfortunately, in spite of their extreme luminosities, individual Population III (Pop III) stars will likely remain beyond the reach of direct observation for decades to come. However, their properties could be revealed by their supernova explosions, which may soon be detected by a new generation of near-IR (NIR) observatories such as *JWST* and WFIRST. We present light curves and spectra for Pop III pair-instability supernovae calculated with the Los Alamos radiation hydrodynamics code RAGE. Our numerical simulations account for the interaction of the blast with realistic circumstellar envelopes, the opacity of the envelope, and Lyman absorption by the neutral intergalactic medium at high redshift, all of which are crucial to computing the NIR signatures of the first cosmic explosions. We find that *JWST* will detect pair-instability supernovae out to $z \gtrsim 30$, WFIRST will detect them in all-sky surveys out to $z \sim 15$ –20, and LSST and Pan-STARRS will find them at $z \lesssim 7$ –8. The discovery of these ancient explosions will probe the first stellar populations and reveal the existence of primitive galaxies that might not otherwise have been detected.

Key words: early universe – galaxies: high-redshift – hydrodynamics – radiative transfer – shock waves – stars: early-type – supernovae: general

Online-only material: color figures

1. INTRODUCTION

Population III (Pop III) stars are the key to understanding primeval galaxies (Johnson et al. 2008, 2009; Greif et al. 2008, 2010; Jeon et al. 2012; Pawlik et al. 2011, 2013; Wise et al. 2012), the chemical enrichment and reionization of the early intergalactic medium (IGM; Smith & Sigurdsson 2007; Smith et al. 2009; Chiaki et al. 2013; Ritter et al. 2012; Safranek-Shrader et al. 2013), and the origin of supermassive black holes (Bromm & Loeb 2003; Johnson & Bromm 2007; Djorgovski et al. 2008; Milosavljević et al. 2009; Alvarez et al. 2009; Lippai et al. 2009; Tanaka & Haiman 2009; Park & Ricotti 2011, 2012; Johnson et al. 2012, 2013c; Whalen & Fryer 2012; Agarwal et al. 2012; Park & Ricotti 2013; Latif et al. 2013a, 2013b; Schleicher et al. 2013; Choi et al. 2013). Unfortunately, even though they are thought to be extremely luminous (Schaerer 2002), individual Pop III stars will not be visible to the *James Webb Space Telescope* (*JWST*; Gardner et al. 2006), the Wide-Field Infrared Survey Telescope (WFIRST), or the Thirty-Meter Telescope (TMT; but see Rydberg et al. 2013 on the possibility of detecting Pop III star H II regions by strong gravitational lensing).

Numerical simulations suggest that the first stars are born in 10^5 – 10^6 M_\odot dark matter halos at $z \sim 20$ –30. The original models implied that they are 100–500 M_\odot and form in isolation, one per halo (Bromm et al. 1999, 2002; Abel et al. 2000, 2002; Nakamura & Umemura 2001; O’Shea & Norman 2007; Yoshida

et al. 2008), but newer models have since shown that some Pop III stars form in binaries (Turk et al. 2009) and perhaps even in small clusters (Stacy et al. 2010; Clark et al. 2011; Greif et al. 2011, 2012; Susa 2013). Simulations of UV breakout from primordial star-forming disks find that radiative feedback limits the final masses of some Pop III stars to $\lesssim 40 M_\odot$ (Hosokawa et al. 2011, 2012; Stacy et al. 2012; but also see Omukai & Palla 2001, 2003; Omukai & Inutsuka 2002; Tan & McKee 2004; McKee & Tan 2008; Hirano et al. 2013). However, none of these models realistically bridge the gap between the formation and fragmentation of the protostellar disk and its evaporation up to a Myr later and they rely on uniform accretion rates and simple recipes for protostellar evolution. For these reasons, and because the roles of turbulence (Latif et al. 2013b), magnetic fields (Schober et al. 2012), and radiation transport in the formation and evolution of primordial disks are not understood, numerical models cannot yet constrain the Pop III initial mass function (IMF; for recent reviews, see Whalen 2012; Glover 2013).

Some have tried to infer the masses of Pop III stars from their nucleosynthetic imprint on later generations, some of which may live today as dim metal-poor stars in the Galactic halo (e.g., Beers & Christlieb 2005; Frebel et al. 2005; Caffau et al. 2012). The current consensus is that 15–40 M_\odot Pop III stars die in core-collapse supernovae (CC SNe) and 140–260 M_\odot stars explode as far more energetic pair-instability (PI) SNe, with up to 100 times the energy of Type Ia or Type II explosions

(Heger & Woosley 2002). Joggerst et al. (2010, hereafter JET10) recently found that the yields of 15–40 M_{\odot} Pop III CC SNe are consistent with the chemical abundances measured in a sample of ~ 130 extremely metal-poor stars (Cayrel et al. 2004; Lai et al. 2008). But traces of the distinctive “odd–even” nucleosynthetic fingerprint of Pop III PI SNe have now been found in high-redshift damped Lyman alpha absorbers (Cooke et al. 2011). Eighteen low-metallicity stars recently discovered in the Sloan Digital Sky Survey have also been designated for further spectroscopic follow-up because they too are suspected to exhibit this pattern (Ren et al. 2012; see also Karlsson et al. 2008 on why the odd–even effect may not have been found in earlier surveys). This new evidence from the fossil abundance record indicates that both low-mass and very massive Pop III stars existed in the early universe. Several stars above the classical 150 M_{\odot} limit have also now been discovered at metallicities $Z \sim 0.1 Z_{\odot}$ in the R136 cluster, including one 300 M_{\odot} candidate, further corroborating the possibility of very massive star formation (Crowther et al. 2010).

Detections of Pop III SNe will be the most direct probe of the first stars in the near term because they are thousands of times brighter than their progenitors and the primitive galaxies that host them (Bromm et al. 2003; Kitayama & Yoshida 2005; Greif et al. 2007; Whalen et al. 2008c; de Souza et al. 2011a; Vasiliev et al. 2012; Pan et al. 2012b). PI SNe in particular are ideal candidates for finding Pop III stars because of their extreme luminosities. Besides the newest results from the fossil abundance record, other new discoveries suggest that PI SNe are more frequent at high redshifts than previously thought. It is now known that rotating Pop III stars can die as PI SNe at masses as low as 85 M_{\odot} (Yoon et al. 2006; Chatzopoulos & Wheeler 2012; Yoon et al. 2012). Assuming simple power-law IMFs, this could increase PI SN rates in the early universe by a factor of 4 (see also Ekström et al. 2008; Stacy et al. 2011, 2013, on the effects of rotation and magnetic fields on Pop III star evolution). Perhaps the most compelling evidence is that a PI SN candidate has now been discovered in the local universe (SN 2007bi, Gal-Yam et al. 2009; Young et al. 2010), in environments that are far less favorable to the formation of massive progenitors than at early epochs (although see Kasen & Bildsten 2010; Dessart et al. 2012, for alternative interpretations of this event).

Previous studies have addressed detection thresholds for PI SNe at $z \sim 5$ (Scannapieco et al. 2005), $6 < z < 15$ (Pan et al. 2012a), and $z \sim 30$ (in approximate terms; Hummel et al. 2012; see also Kasen et al. 2011; Dessart et al. 2013; de Souza et al. 2013). The interaction of the PI SN with its envelope, the opacity of the envelope, and Lyman absorption by the neutral IGM at early epochs must all be taken into account to calculate its near-IR (NIR) signature at high redshift. Doing so, Whalen et al. (2013b) found that *JWST* will detect PI SNe out to $z \sim 30$. However, their models did not cover the full range of stellar structures expected for 140–260 M_{\odot} Pop III stars. We have now calculated Pop III PI SNe for both blue giants and red hypergiants at $7 < z < 30$ with the Los Alamos RAGE and SPECTRUM codes. In Section 2, we review the PI explosion mechanism, the presupernova structures of the stars, and our Kepler Pop III PI progenitor and SN models. We describe our RAGE and SPECTRUM source frame light curve and spectrum calculations in Section 3, and we examine PI SN blast profiles and spectra in Section 4. In Section 5, we present Pop III PI SN NIR light curves and determine their detection limits as a function of redshift. In Section 6, we discuss PI SN detection rates at $5 < z < 30$, and we conclude in Section 7.

2. PI SN MODELS

PI SNe were first proposed by Rakavy & Shaviv (1967) and Barkat et al. (1967) and have been studied numerous times since then (see Heger & Woosley 2002 and references therein). Pop III stars above 65 M_{\odot} encounter the pair instability after central carbon burning, when thermal energy creates e^+e^- pairs rather than maintaining pressure support against collapse. The cores of these stars subsequently contract, triggering explosive thermonuclear burning of O and Si. Above 140 M_{\odot} , the energy that is released completely unbinds the star, and no black hole is formed. At 260 M_{\odot} the core of the star reaches temperatures that are high enough for alpha particles to be photo-disintegrated into free nucleons, which consumes as much energy per unit mass as was released by all preceding burning. The star collapses instead of exploding. PI SNe are the most energetic thermonuclear events in the universe, with yields of up to 10^{53} erg for 260 M_{\odot} stars.

The early spectral signatures of Pop III PI SNe heavily depend on the radius and structure of the star in addition to the explosion energy, the interaction of the blast with the envelope, the opacity of the envelope, and absorption by the IGM. Shock temperatures at breakout are lower for large stars than for compact stars of equal mass because the shock has expanded to a greater radius and done more work on its environment. Early spectra from the explosions of compact blue stars are therefore harder than those of red giants. As we discuss below, the structure of the star also determines the emission lines that appear in its spectra over time. The size and structure of the progenitor in turn are governed by its metallicity and by internal convection over its life.

2.1. Semi-Convective Mixing

Convection can determine if a very massive Pop III star dies as a compact blue giant or a red hypergiant. As described in detail in Scannapieco et al. (2005), the convection zone of the star can approach, touch, or even penetrate the lower hydrogen layers, mixing them with carbon dredged up from the core from He burning. When these two high-temperature components mix, they burn violently, boosting energy production rates in the H shell by up to several orders of magnitude. This, together with the now greater opacity of the lower hydrogen layer, can puff up the star by more than an order of magnitude in radius.

2.2. Metallicity

Gas in high-redshift halos that is enriched to metallicities below $10^{-3.5} Z_{\odot}$ fragments on mass scales that are essentially identical to those of pristine gas and forms very massive stars (e.g., Bromm et al. 2001; Mackey et al. 2003; Smith & Sigurdsson 2007). However, these low metallicities are more than enough to enhance CNO reaction and energy production rates in the hydrogen-burning layers of the star, inflating the stellar envelope as much as convection. Since there is a strong degeneracy between the effects of metals and convection on the structure of the star, the full range of light curves and spectra for Pop III PI SNe is as easily spanned by metallicity as by convective overshoot, as we demonstrate below.

2.3. Explosive Mixing

JET10 found that in 15–40 M_{\odot} Pop III SNe the shock completely disrupts the interior of the star, heavily mixing the ejecta by the time it ruptures the surface. In contrast, the

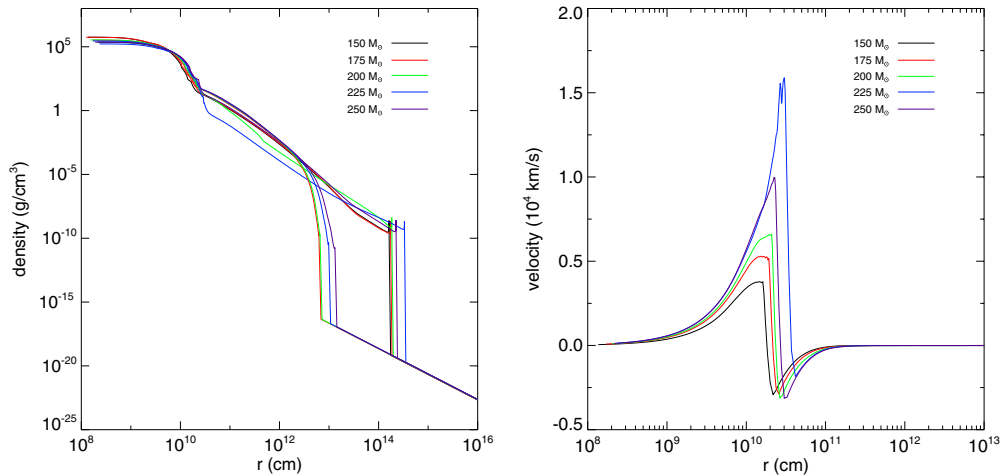


Figure 1. Kepler PI SN explosion and stellar envelope profiles. Left panel: densities for all nine models. The surface of each star is marked by the abrupt drop in density by 10 orders of magnitude at $r \sim 10^{13}$ cm in the four z-series profiles and a few $\times 10^{14}$ cm in the five u-series stars. A wind with a total mass of $0.1 M_{\odot}$, a velocity of 10^8 cm s $^{-1}$, and a free-streaming r^{-2} profile is extended from the surface of the star out to the uniform relic H II region surrounding the star, which is not visible on this plot. Right panel: velocity profiles for the u-series stars. Both the outgoing shock and ongoing collapse of the outer layers of the star are visible. (A color version of this figure is available in the online journal.)

concentric shells of elements expand almost homologously in PI SNe with only occasional minor mixing between the O and He layers prior to breakout (Joggerst & Whalen 2011; see also Chen et al. 2011). Mixing in the star during the explosion can determine the order in which elements appear in emission lines over time. In the frame of the shock, the photosphere from which photons escape descends into the ejecta over time as each fluid element expands and the ejecta is diluted. If Rayleigh–Taylor instabilities drive mixing prior to shock breakout, they can dredge heavy elements from a deeper mass coordinate up to the photosphere and expose them to the IGM at much earlier times. Since mixing is minimal in Pop III PI SNe, the absence of metal lines soon after breakout would be one of several markers of the event.

2.4. Kepler

To model the structure of the progenitor, we evolve 150, 175, 200, 225, and 250 M_{\odot} zero-metallicity stars (z-series) and $10^{-4} Z_{\odot}$ stars (u-series) from the zero age main sequence to the onset of collapse in the one-dimensional (1D) Lagrangian stellar evolution code Kepler (Weaver et al. 1978; Woosley et al. 2002). The explosion begins when this collapse triggers rapid O and Si burning. Unlike the CC SN simulations of JET10, in which the blast must be artificially launched with a piston and the explosion energy is a free parameter, the PI SN is an emergent feature of our stellar evolution model, and its energy is set by how much O and Si burns. The blast was followed until the end of all nuclear burning at ~ 20 s, when the shock was still deep inside the star. We calculate energy generation with a 19-isotope network up to the point of oxygen depletion in the core and with a 128-isotope quasi-equilibrium network thereafter. The z-series 150 M_{\odot} star collapses to a black hole without an explosion. The number of mass zones on the grid ranged from 1000 to 1200 and was always sufficient to resolve all salient structures of the star and SN. We show density and velocity profiles for our explosions in Figure 1 and summarize our grid of models in Table 1. We consider only non-rotating progenitors.

We use metallicity rather than convective overshoot to parameterize the progenitors because for a given star the size

Table 1
Kepler PI SN Models (Masses are in M_{\odot})

Model	M_{He}	R (10^{13} cm)	E (10^{51} erg)	$M_{56\text{Ni}}$
u150	72	16.2	9.0	0.07
u175	84.4	17.4	21.3	0.70
u200	96.7	18.4	33	5.09
u225	103.5	33.3	46.7	16.5
u250	124	22.5	69.2	37.9
z175	84.3	0.62	14.6	0
z200	96.9	0.66	27.8	1.9
z225	110.1	0.98	42.5	8.73
z250	123.5	1.31	63.2	23.1

of the central convection zone is uncertain but $Z = 0$ and $10^{-4} Z_{\odot}$ bracket the metallicities over which 140–260 M_{\odot} Pop III stars are expected to form (Mackey et al. 2003; Smith & Sigurdsson 2007; Smith et al. 2009). As we show in Figure 1, these two metallicities yield blue giant and red hypergiant envelopes similar to those obtained by varying convective mixing in Scannapieco et al. (2005). All u-series stars in our study die as red hypergiants, and all z-series stars die as blue giants. The light curves and spectra for our SNe should therefore bracket those that will be observed (but most 140–260 M_{\odot} Pop III stars are thought to have convective mixing and die as red stars rather than blue stars).

3. RAGE AND SPECTRUM SIMULATIONS

We propagate the shock through the interior of the star, its surface, and then out into the surrounding medium with the radiation hydrodynamics code RAGE (Gittings et al. 2008). RAGE (Radiation Adaptive Grid Eulerian) is a multidimensional adaptive mesh refinement (AMR) radiation hydrodynamics code developed at Los Alamos National Laboratory (LANL). RAGE couples second-order conservative Godunov hydrodynamics to gray or multigroup flux-limited diffusion (FLD) to model strongly radiating flows. RAGE utilizes the extensive LANL OPLIB database of atomic opacities¹¹

¹¹ <http://aphysics2.lanl.gov/opacity/lanl>

(Magee et al. 1995) and can also evolve multimaterial flows with a variety of equations of state (EOS). We describe most of the physics implemented in our RAGE models and why it is needed to capture the features of our light curves in detail in Frey et al. (2013, hereafter FET12): multispecies advection, gray FLD radiation transport with two-temperature (2T) physics, and energy deposition by radioactive decay of ^{56}Ni . In particular, 2T radiation transport, in which radiation and matter temperatures are evolved separately, better models shock breakout and its aftermath when matter and radiation can be out of equilibrium. This is an important improvement over earlier 1T models of PI SN explosions. We evolve mass fractions for 15 elements, the even numbered elements predominantly synthesized in PI SNe.

3.1. Self-Gravity

We have also now implemented self-gravity in RAGE, which was not included in the Whalen et al. (2013b) models. Although they are extremely energetic, PI SN shocks are launched from deep inside the star where the gravitational potential energy of the ejecta is quite large. If this energy is not taken into account, the shock can break out of the star with too large a velocity and luminosity. Gravity was implemented in spherical symmetry by computing the potential

$$\phi = -\frac{GM_{\text{encl}}}{r}, \quad (1)$$

where

$$M_{\text{encl}} = \int_0^r 4\pi r'^2 \rho(r') dr' \quad (2)$$

is constructed by extracting the densities from the finest levels of the AMR hierarchy and reordering them by radius. The gravitational potential is then applied to updates to the gas velocities and total energies every time step.

We tested gravity by running a pressureless sphere collapse problem with an analytical solution. If the sphere has the density profile

$$\rho(r) = \frac{\alpha}{r}, \quad (3)$$

then $M_{\text{encl}} = 2\pi\alpha r^2$ and in the absence of pressure forces each spherical shell experiences a constant acceleration a given by

$$a = -\frac{GM_{\text{encl}}}{r^2} = -2\pi\alpha G. \quad (4)$$

The sphere collapses homologously with a velocity $v = -2\pi\alpha Gt$. We show a snapshot of radial velocities for the collapse of the sphere for $\alpha = 10^4$ at 100 s in Figure 2. The sphere is zoned into 10,000 uniform mesh points with reflecting inner boundary conditions, an outer boundary at 10^9 cm, a resolution of 10^5 cm, and $v_{\text{init}} = 0$. Although it is not possible to disable pressure forces in RAGE, we make them negligible by reducing the heat capacity C_V from the usual 1.2472×10^8 erg K $^{-1}$ for an ideal gas to 1.0 erg K $^{-1}$.

As shown in Figure 2, RAGE agrees with the analytical solution to within 1% beyond 10^7 cm, with at most 10% error at the inner boundary where gas begins to pile up. The departures from the analytic solution there are due to residual pressure forces that build up in the increasingly dense gas. In this test problem RAGE conserves total energy (gravitational + kinetic + internal) to within machine precision.

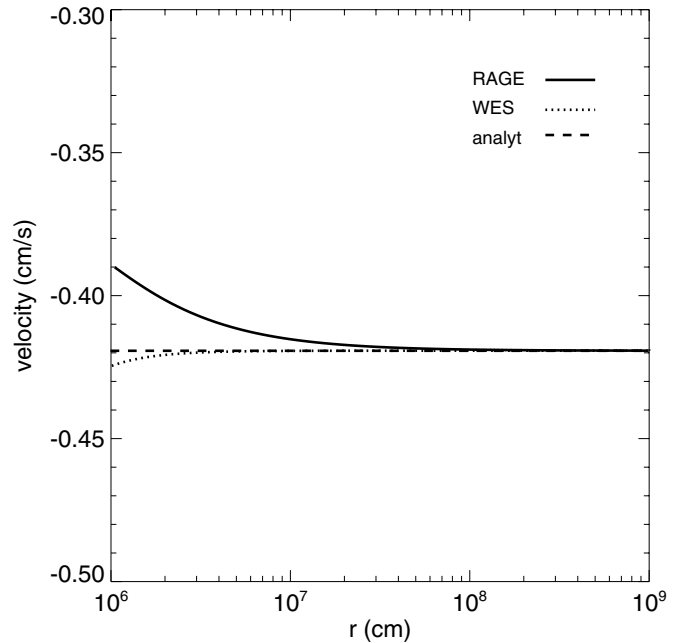


Figure 2. Collapse test for the pressureless sphere with $\alpha = 10^4$. Velocities are shown as a function of radius at $t = 100$ s ($v_{\text{an}} = -0.419$ cm s $^{-1}$) for RAGE and a semi-analytic code versus the analytical solution.

3.2. Initial Grid

We map densities, velocities, specific internal energies (erg gm $^{-1}$), and species mass fractions for the explosion and star from Kepler together with a circumstellar envelope onto a uniform 50,000-zone 1D spherical mesh in RAGE. Since radiation energy densities are not explicitly evolved in the Kepler models, we initialize them in RAGE as

$$e_{\text{rad}} = aT^4, \quad (5)$$

where $a = 7.564 \times 10^{-15}$ erg cm $^{-3}$ K $^{-4}$ is the radiation constant and T is the gas temperature. Also, because the gas energy in Kepler includes contributions by ionization states of atoms, we unambiguously construct the specific internal energy from T with

$$e_{\text{gas}} = C_V T, \quad (6)$$

where $C_V = 1.2472 \times 10^8$ erg K $^{-1}$ is the specific heat of the gas. Since there is little mixing in the star as the shock propagates to the surface, the radial distribution of elements in the star is essentially frozen in mass coordinate at death and expands homologously into space thereafter. 1D simulations are therefore sufficient to capture the key attributes of PI SN light curves and spectra.

At the beginning of the simulation we allocate 5000 zones from the center of the grid to the edge of the shock in the velocity profile. We allow up to five levels of refinement in the initial interpolation of the profile onto this grid and then throughout the simulation. Our choice of grid ensures that the photosphere of the ejecta is always fully resolved, since failure to do so can lead to luminosity underestimates during post-processing. We impose reflecting and outflow boundary conditions on the fluid and radiation flows at the inner and outer boundaries of the mesh, respectively.

When the calculation is begun, Courant times are initially small due to high temperatures, large velocities, and small

cell sizes. To reduce execution times and to accommodate the expansion of the ejecta, we periodically regrid the profiles onto a larger mesh as described in detail in FET12. Each time we regrid the blast we allocate 5000 zones out to either the edge of the shock (pre-breakout) or the edge of the radiation front (post-breakout—we take the edge of the front to be where the radiation temperature falls to a few tenths of an eV. Up to five levels of refinement are used during the regrid and then again during the simulation. The inner boundary is always at 0 cm, and the outer boundary of the final, largest mesh in our models is 1.0×10^{18} cm. We assume that the final mass of each star is the same as its initial mass.

3.3. Circumstellar Winds

Pop III stars are usually thought to die in low-density H II regions with relatively flat density profiles $n \sim 0.1\text{--}1\text{ cm}^{-3}$ out to 100–200 pc (Whalen et al. 2004; Kitayama et al. 2004; Alvarez et al. 2006; Abel et al. 2007; Wise & Abel 2008a; Whalen & Norman 2008b, 2008a). They are not believed to lose much mass over their lifetimes because there are no metals in their atmospheres to drive strong winds (Kudritzki 2000; Baraffe et al. 2001; Vink et al. 2001; Krtićka & Kubát 2006; Ekström et al. 2008). However, we allow for the possibility that some Pop III stars have winds. First, mass loss from very massive stars is usually just parameterized by metallicity, not calculated from first principles with radiation hydrodynamics (e.g., Meynet et al. 1994). Extrapolating no winds at zero metallicity could exclude mass loss by other means, such as helium opacity, hydromagnetic flows, or pulsational ejections (Heger & Woosley 2002). Second, mixing in rotating Pop III stars, which we do not consider here, can dredge metals up from the interior of the star to its surface and drive winds later in its life (e.g., Ekström et al. 2008), although the mass loss so far has been found to be minor. Lastly, there are no observations to rule out winds from very massive zero-metallicity stars. We therefore extend a low-mass wind profile from the surface of the star out to the relic H II region:

$$\rho_w(r) = \frac{\dot{m}}{4\pi r^2 v_w}, \quad (7)$$

where \dot{m} is the mass-loss rate due to the wind and v_w is the wind speed. The mass-loss rate is

$$\dot{m} = \frac{M_{\text{tot}}}{t_{\text{MSL}}}, \quad (8)$$

where M_{tot} and t_{MSL} are the total mass loss and lifetime of the star, respectively. We take $M_{\text{tot}} = 0.1 M_{\odot}$, $v_w = 1000\text{ km s}^{-1}$, and $T_w = 0.01\text{ eV}$ in all our models. The wind is H and He only, with mass fractions of 76% and 24%, respectively. The radius at which the density of the wind is joined to the H II region, whose density we take to be 0.1 cm^{-3} , varies with the radius of each star but is typically $10^{17}\text{--}10^{18}$ cm. Density and velocity profiles for the wind are visible in Figure 1.

3.4. Ionization of the Wind

To determine if the progenitor ionizes the wind, we use the ZEUS-MP code to model the propagation of the ionization front from the surface of the star (Whalen & Norman 2006, 2008a, 2008b). We center a blue $175 M_{\odot}$ z-series star in the wind on a 1D spherical mesh with 200 zones and inner and outer

boundaries at 7.0×10^{12} cm and 1.0×10^{15} cm, respectively (the surface of the star and the outer regions of the wind). To enhance grid resolution in the densest regions of the wind, we use logarithmically ratioed zones, where

$$\frac{\Delta r_{i+1}}{\Delta r_i} = 1.043. \quad (9)$$

We evolve the I-front with multifrequency UV transport, with 40 bins uniformly partitioned in energy from 0.255 to 13.6 eV and 80 logarithmically spaced bins from 13.6 to 90 eV. We take the spectrum of the star to be blackbody, normalized to ionizing photon rates, surface temperatures, and luminosities from Schaerer (2002).

The star easily ionizes the wind on timescales of $\sim 10^4$ yr. The gas temperature is 40,000 K near the surface of the star, where rapid ionizations and recombinations in the large fluxes and densities there lead to greater heating than at 10^{15} cm, where temperatures are $\sim 25,000$ K. Because the least massive blue star in our study easily ionizes the wind (and has the highest surface wind density), we conclude that the winds around all z-series progenitors in our simulations are ionized.

Red u-series progenitors have surface temperatures that are too low to emit ionizing UV but still ionize their wind envelopes because they are blue for most of their lives. They become too cool to sustain ionizing flux only in their final few hundred kyr. Recombination times in the wind therefore determine its ionization state when the star dies, without the need for a transport calculation:

$$t_{\text{rec}} = \frac{1}{n_e \alpha(T)}. \quad (10)$$

Here, n_e is the electron number density and $\alpha(T)$ is the recombination rate coefficient for hydrogen, which we take to be $2.59 \times 10^{-13} T_4^{-0.75} \text{ s}^{-1}$, where T_4 is the temperature in units of 10^4 K. With the ionized gas temperatures we found for the compact $175 M_{\odot}$ star and the densities of the modest winds in our study, recombination times vary from 5 to 50 kyr in the vicinity of the star, ensuring that the wind is neutral when the star explodes. For simplicity, we take the wind to be neutral around all the stars in our study, so our luminosities at shock breakout for z-series stars will be lower limits because neutral envelopes allow less flux to escape until they are fully ionized by the breakout pulse. We note that the ionized wind itself has significant luminosity due to recombinations (Rydberg et al. 2010), but we are primarily interested in the transient flux from the explosion, not the steady emission from its envelope.

3.5. SPECTRUM

To calculate a spectrum from a RAGE profile, we map its densities, temperatures, mass fractions, and velocities onto a new grid in the SPECTRUM code. SPECTRUM performs a direct sum of the luminosity of every fluid element in this discretized snapshot to compute the total flux that exits the ejecta along the line of sight at every wavelength. This procedure, described in detail in FET12, accounts for Doppler shifts and time dilation due to relativistic expansion of the ejecta. We also calculate the intensities of emission lines and attenuation of flux along the line of sight with monochromatic OPLIB opacities, thereby capturing both limb darkening and the absorption lines imprinted on the flux by intervening material in the ejecta and wind.

As explained in FET12, gas densities, velocities, mass fractions, and radiation temperatures from the finest levels of refinement of the RAGE AMR grid are first extracted and ordered by radius into separate files, one variable per file. In these runs, the profiles have 50,000 radial zones, and constraints on machine memory and time prevent us from using all of them to calculate spectra, so only a subset of the points is mapped onto the SPECTRUM grid. We first sample the RAGE radiation energy density profile inward from the outer boundary to find the position of the radiation front, which we take to be where aT^4 rises above 1.0 erg cm^{-3} . We then find the radius of the $\tau = 25$ surface by integrating the optical depth due to Thomson scattering inward from the outer boundary ($\kappa_{Th} = 0.288$ for H and He gas at primordial composition). This yields the greatest depth in the ejecta from which photons can escape because κ_{Th} is the minimum opacity the photons would encounter.

The extracted densities, velocities, temperatures, and species mass fractions from RAGE are then interpolated onto a two-dimensional (2D) grid in r and θ in SPECTRUM whose inner and outer boundaries are 0 and 10^{18} cm , respectively. Eight hundred uniform zones in log radius are allocated from the center of the grid to the $\tau = 25$ surface. The region between the $\tau = 25$ surface and the edge of the radiation front is partitioned into 6200 uniform zones in radius. The wind between the front and the outer boundary of the grid is then divided into 500 uniform zones in log radius, for a total of 7500 radial bins. The data in each of these new radial bins are mass-averaged to ensure that SPECTRUM captures very sharp features from the RAGE profile. The grid is uniformly discretized into 160 bins in $\mu = \cos \theta$ from -1 to 1 . Our choice of mesh yielded good convergence in spectrum tests, fully resolving regions of the flow from which photons can escape the ejecta and only lightly sampling those from which they cannot.

Summing the luminosities at each wavelength in one spectrum yields the bolometric luminosity of the SN at that moment. Many such luminosities computed over a range of times constitute the light curve of the explosion. We sample the light curve with 200–340 spectra that are logarithmically distributed in time out to 3 yr.

4. PI SN BLAST PROFILES, LIGHT CURVES, AND SPECTRA

The onset of explosive burning drives a strongly radiating shock from the O layer into the upper layers of the star, as we show in Figure 3. At this point the shock is not visible to an external observer because its photons are trapped by e^- scattering in the intervening layers, so they are simply advected outward by the fluid flow. The SN becomes visible when the shock breaks through the surface of the star. Shock breakout has been the subject of numerous analytical studies (Colgate 1974; Matzner & McKee 1999; Nakar & Sari 2010; Piro et al. 2010; Katz et al. 2012) and numerical studies (Ensmann & Burrows 1992; Blinnikov et al. 2000; Tominaga et al. 2009; Tolstov 2010; Kasen et al. 2011; Blinnikov & Tolstov 2011; Tolstov et al. 2013) in the past 30 yr but has not been observed until more recently (e.g., Soderberg et al. 2008; Gezari et al. 2008; Schawinski et al. 2008; Dwek & Arendt 2008).

4.1. Shock Breakout

When the shock reaches the surface of the star, it abruptly accelerates to large velocities in the steep density gradient there, as we show in the left panel of Figure 4. The acceleration heats

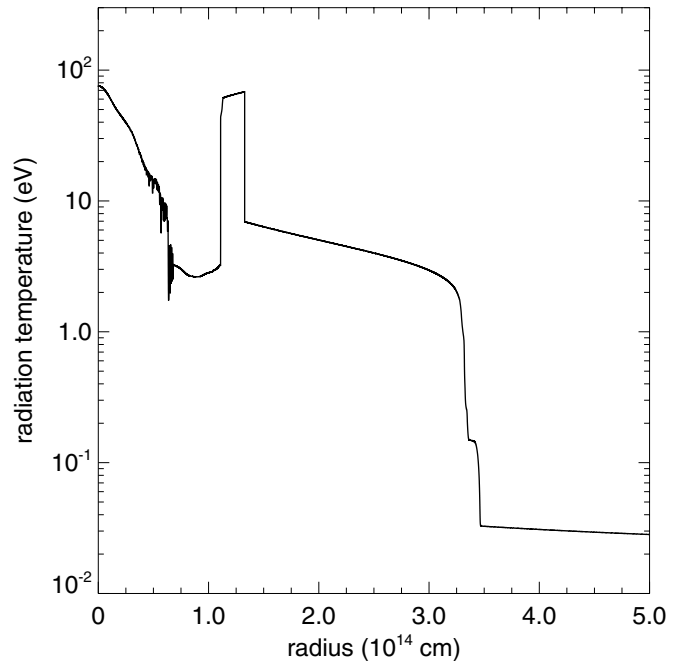


Figure 3. Highly radiative shock in the u225 model at $1.59 \times 10^5 \text{ s}$. The shock is at $1.2 \times 10^{14} \text{ cm}$, deep inside the star. Photons from the shock cannot reach the surface of the star from this depth because of Thomson scattering in its upper layers. The 0.2 eV plateau in the temperature at the stellar surface at $3.2 \times 10^{14} \text{ cm}$ is optical radiation from the star propagating out into the wind before shock breakout.

the shock and it releases an intense burst of photons upon being exposed to the low-density IGM, as shown in the right panel of Figure 4. The advancing radiation front is visible as the 20 eV plateau in gas temperature at $1.2 \times 10^{13} \text{ cm}$ at 3990 s that is 10 eV at $2.0 \times 10^{13} \text{ cm}$ at 4550 s. The plateau temperatures are those to which the radiation front heats the wind as it passes through it; the shock that is emitting the radiation is much hotter, as we show below. The temperature of the plateau falls as the shock expands and, cools and its spectrum softens. Note that there are serious departures from self-similarity in the velocity profiles at late stages of breakout (third plot in the left panel of Figure 4) because of significant coupling between radiation and gas in the shock. This is one reason Sedov–Taylor profiles are not good solutions for shock breakout (Fryer et al. 2010) and why radiation transport is required to model the flow.

We show bolometric luminosities for the breakout transient for the u-series and z-series PI SNe in the left and right panels of Figure 5, respectively. For comparison, we show the blackbody approximation to the luminosity of the shock for the u225 explosion,

$$L = 4\pi r^2 \sigma T^4, \quad (11)$$

where σ is the Stefan–Boltzmann constant and the temperature T of the shock is taken at the $\tau_{Th} = 1$ surface, where $\kappa_{Th} = 0.288$. If photons of all energies broke through the surface of the star at the same time, the duration of the initial transient would be comparable to the light-crossing time of the star, since photons emitted from its poles and its equator would reach an observer at times that differ by the time it takes light to cross the star. Given that u-series stars have radii of a few $\times 10^{14} \text{ cm}$, their breakout transients would last 1–2 hr, which is consistent with the width of the $4\pi r^2 \sigma T^4$ approximation to the luminosity of the pulse. In reality, the transient is smeared out over longer times because radiation remains strongly coupled to the shock past breakout

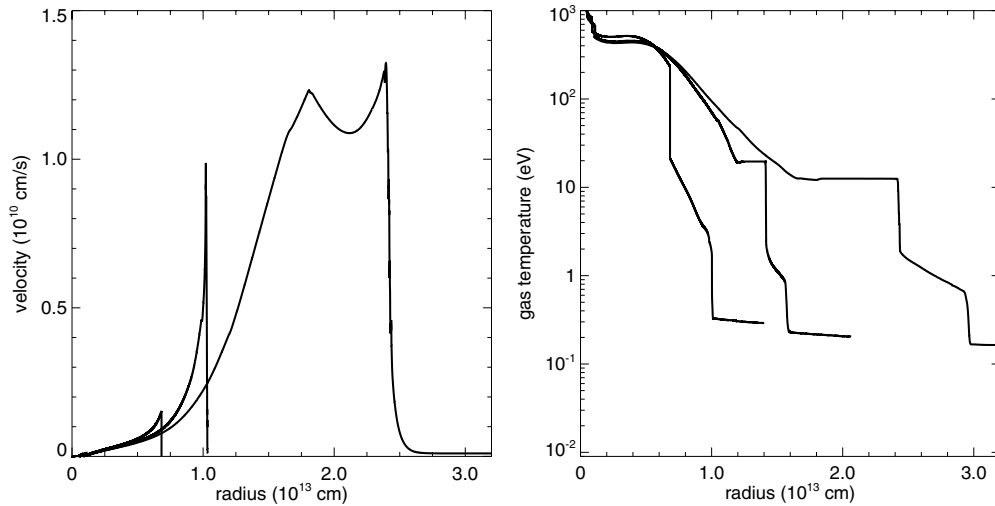


Figure 4. Shock breakout in the z225 explosion. Left panel: velocities, from left to right, at 8309 s, 9325 s, and 9962 s. Shock breakout through the surface of the star is evident in the abrupt jump in velocity in the second profile, and the continued acceleration of the shock down the r^{-2} density profile of the wind is visible in the third profile. Right panel: gas temperatures at 8309 s, 9502 s, and 9962 s from left to right. The radiation breakout pulse is the flat 20 eV plateau in gas temperature at 1.2×10^{13} cm at 9502 s. As the shock expands and cools, the spectrum of the breakout pulse softens, which is why the gas temperature in its wake has fallen to ~ 10 eV at 9962 s.

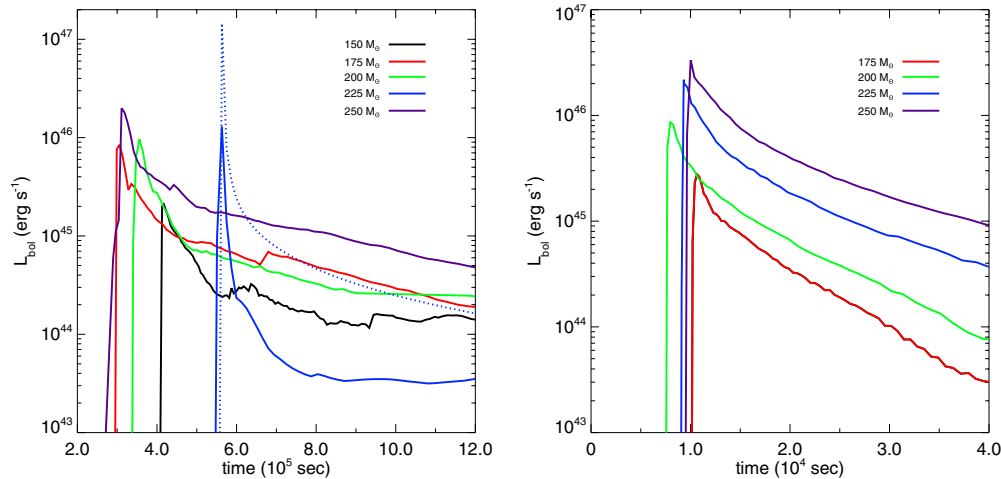


Figure 5. Bolometric luminosities. Left panel: u-series PI SNe. The dotted blue line is the blackbody approximation to the u225 light curve (Equation (11)). Right panel: z-series PI SNe.

(A color version of this figure is available in the online journal.)

(as shown in the third velocity profile in Figure 4). The resulting pulse is dimmer but longer. The width of the transient is much greater for giant red u-series stars because of their larger radii, lower surface densities, and thus broader regions from which photons break free of the shock.

We show spectra for the breakout pulse for u250 and z250 PI SNe in the left and right panels of Figure 6, respectively. The z250 transient is mostly X-rays, and the u250 pulse is both X-rays and hard UV. The spectrum of the u250 transient is softer because the progenitor is much larger and the shock has done more PdV work on its surroundings and cooled more by the time it breaks out of the star. The ionization of the surrounding wind envelope is particularly evident in the z250 breakout spectra, as the prominent absorption features at 9652 s are mostly gone by 1.40×10^4 s. By the end of shock breakout the surrounding wind is completely ionized by the radiation pulse and the spectrum of the shock has essentially a blackbody profile.

Peak bolometric luminosities vary from 8×10^{45} to 3×10^{46} erg s $^{-1}$, or ~ 200 times the luminosity of our Galaxy.

These peak luminosities are consistent with those of Kasen et al. (2011), which were computed with the Kepler and SEDONA codes utilizing the Lawrence Livermore OPAL opacities (Iglesias & Rogers 1996; Rogers et al. 1996).¹² There is a general trend of greater luminosity with explosion energy and later breakout times with progenitor mass, since stellar radii increase with mass. Although the shock has a much smaller radius at breakout in the z-series than in the u-series, it has about the same total luminosity because it is hotter. This can be seen from how the luminosity L of a blackbody scales with radius and temperature in Equation (11). Typical shock temperatures at the $\tau = 1$ surface at breakout are ~ 500 eV in the z-series stars and ~ 50 eV in the u-series stars, which roughly compensates for the factor of 10 in radius between the two progenitors.

However, we note that the luminosity of the shock is not well approximated by that of a blackbody and that it is roughly an order of magnitude below that predicted by Equation (11),

¹² <http://rdc.llnl.gov>

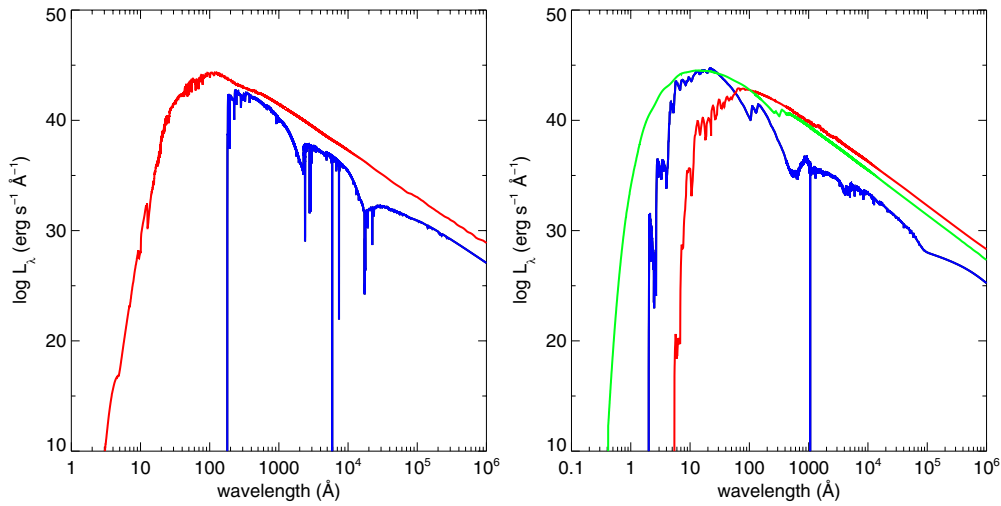


Figure 6. Spectra of the breakout transient. Left panel: u250 explosion. Blue: 2.90×10^5 s; red: 3.11×10^5 s. Right panel: z250 explosion. Blue: 9652 s; green: 1.40×10^4 s.

(A color version of this figure is available in the online journal.)

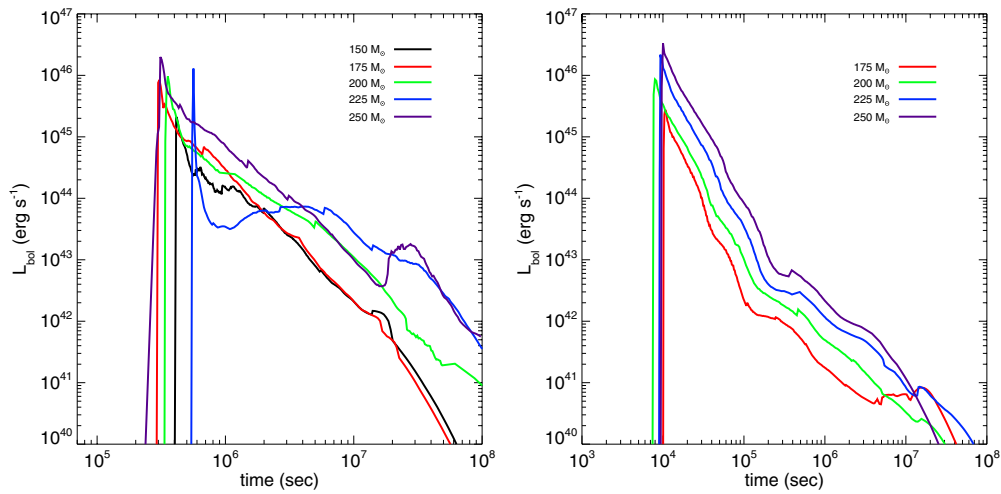


Figure 7. Source-frame bolometric luminosities for all nine PI SNe out to three yr. Left panel: u-series. Right panel: z-series. The general trend of higher luminosity with progenitor mass in each series is evident, as is the fact that u-series explosions are brighter than z-series SNe of equal progenitor mass. The resurgence in luminosity at $\sim 10^7$ s in most of the SNe coincides with the descent of the photosphere of the shock into the hot ^{56}Ni layer of the ejecta.

(A color version of this figure is available in the online journal.)

as we show in Figure 5.¹³ Treating SN shocks as blackbodies in general can lead to overestimates in luminosity of an order of magnitude or more at breakout, as discussed in Fryer et al. (2010). One aspect of shock breakout that is unique to our study is that it is redshifted from 1 to 2 hr in duration at $z \sim 20$ to a day or more in the observer frame. This would enhance the probability of detecting ancient SNe if not for the fact that the transient is completely absorbed by the neutral IGM at high redshift.

4.2. Intermediate/Late Stages of the SN

We show bolometric light curves out to three years for the u-series and z-series SNe in the left and right panels of Figure 7, respectively. PI SN luminosities are powered at early times by the conversion of kinetic and radiation energy into thermal

energy by the shock, so they are far brighter than Type Ia and II SNe at this stage because they have much higher explosion energies. At later times their luminosity comes mostly from radioactive decay, and they are much brighter than other SNe because they synthesize more ^{56}Ni : up to $40 M_{\odot}$ compared to $0.4\text{--}0.8 M_{\odot}$ and $<0.3 M_{\odot}$ in Type Ia and Type II SNe, respectively. They are brighter for longer times (three yr instead of three to six months for Type Ia and II SNe) because radiation diffusion timescales in their more massive ejecta are much longer:

$$t_d \sim \kappa^{\frac{1}{2}} M_{ej}^{\frac{3}{4}} E^{-\frac{3}{4}}. \quad (12)$$

Here, κ is the average opacity of the ejecta, M_{ej} is the mass of the ejecta, and E is the explosion energy. The luminosity generally rises with progenitor mass within each series because the explosion energy and ^{56}Ni mass increase with stellar mass in both red and blue stars. All five u-series explosions exhibit a slower, more protracted decay in luminosity out to four months than the z-series SNe and are more than an order of magnitude brighter over this interval. These profiles are

¹³ Because of e^- scattering in the photosphere of the ejecta, the luminosity of the shock is better modeled by $L = 4\pi\epsilon r^2\sigma T^4$, where $\epsilon < 1$ is the correction to the blackbody luminosity due to scattering.

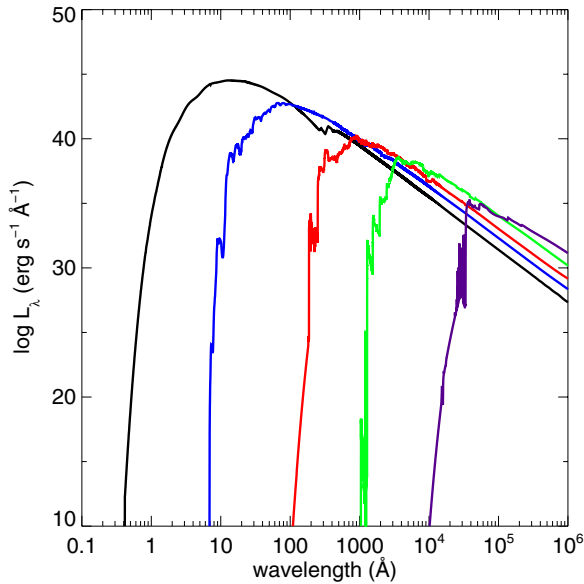


Figure 8. Spectral evolution of the z250 PI SN. Fireball spectra at 1.40×10^4 s (black), 4.77×10^4 s (blue), 2.10×10^5 s (red), 1.95×10^6 s (green), and 3.39×10^7 s (purple).

(A color version of this figure is available in the online journal.)

consistent with those of Type II plateau SNe, whose progenitors are also thought to be red giants with extended envelopes. Their greater luminosities over this interval are due to the fact that the u-series SN shocks are twice as hot as the z-series shocks, in part because u-series explosions create more ^{56}Ni than z-series SNe for progenitors of equal mass (see Table 1).

There is prominent bump in luminosity at two to four months that lasts for about a year in the u225 and u250 light curves. This rebrightening happens when photons diffusing out from the ^{56}Ni layer deep in the ejecta begin to reach the photosphere and escape into the IGM. The magnitude and duration of the bump are proportional to the ^{56}Ni mass, which explains its absence in the u150 and u175 SNe, which create less than 1/10 of the ^{56}Ni formed in the u225 SN. The escape of photons from the ^{56}Ni layer is visible in the u200 light curve as the inflection upward in luminosity at about one month. Such inflections are also present in all four z-series explosions, which do rebrighten somewhat but much less so than the u-series. The z-series SNe are dimmer at these intermediate times because they create less ^{56}Ni than u-series explosions and because their ^{56}Ni remains deeper in the ejecta.

We show the evolution of the spectra for the z250 PI SN from shock breakout to one yr in Figure 8. Two physical processes govern the evolution of the spectrum over time. First, as the fireball expands, it cools, and its spectral cutoff advances to longer wavelengths over time. Second, the wind envelope that was ionized by the breakout pulse begins to recombine and absorb photons at the high-energy end of the spectrum, as evidenced by the flux that is blanketed by lines at the short-wavelength limit of the spectrum. At later times, flux at longer wavelengths slowly rises due to the expansion of the surface area of the photosphere. Over the wavelength scale of this plot the many thousands of lines captured by the LANL OPLIB opacities in our SPECTRUM calculation are blended together in the prominent jagged spectral features throughout the spectrum. Given how line blanketing by both the ejecta and the wind shears off the spectrum at short wavelengths, it is clear that

the common practice of fitting blackbodies to light curves to approximate spectra overestimates flux at high energies from which many photons are eventually redshifted into the NIR in the observer frame.

We plot velocity and density profiles at 8.36×10^5 s, 7.41×10^6 s, and 7.36×10^7 s for the u250 explosion in the left and right panels of Figure 9. Soon after shock breakout and radiation has decoupled from the outer layers of the star, the velocity profiles of the flow become essentially free expansions and are mostly self-similar until the end of the simulations at three yr. The homologous expansion of the flow is also evident in the densities, although there is some variation in their structure deep in the ejecta over time. This is consistent with Joggerst & Whalen (2011) and Chen et al. (2011), who found that any mixing in the ejecta was complete by shock breakout.

5. POP III PI SN DETECTION THRESHOLDS

We have calculated NIR light curves for our PI SNe with the synthetic photometry code described in Su et al. (2011). Each spectrum is redshifted to the desired value before removing the flux absorbed by intervening neutral hydrogen along the line of sight according to the prescription of Madau (1995). We then dim the spectrum by the required cosmological factors. A variety of instrument filters can be easily accommodated by our code, which linearly interpolates the least-sampled data between the input spectrum and filter curve to match the other. It has additional capabilities such as reddening by dust that are not used here.

5.1. NIR Light Curves

At $z \gtrsim 7$, Lyman absorption by the neutral IGM will absorb most flux at wavelengths blueward of 1216 Å. However, in principle the fireball could be brighter slightly blueward of the Lyman limit rather than redward even with IGM absorption (see Figure 3 in Whalen et al. 2013b). At every redshift for each explosion, we calculate the NIR signal in JWST NIRCams filters above and below the Lyman limit to find the filter in which the SN is brightest. We find that for all the redshifts and PI SNe in our study the explosion is most luminous just redward of 1216 Å in the source frame. We show light curves for our PI SNe at $z = 10, 15, 20$, and 30 in Figures 10 and 11. At each redshift, light curves are plotted only for the filter in which the SN will be brightest. Photometry limits for all four filters are AB magnitude 32. All five u-series explosions are visible for 600–1000 days, even at $z = 30$. The z-series SNe are dimmer and are only visible out to $z = 15$ for at most 100 days. They have lower bolometric and NIR luminosities and dim sooner because they create less ^{56}Ni than the u-series. None of the u-series light curves reach the detection threshold before 50 days, or ~ 1.5 days in the source frame at $z = 30$, so shock breakout cannot be seen from Earth. Likewise, none of the z-series SNe are visible before 10 days, or 16 hr in the source frame. The X-rays and hard UV in the breakout transient are absorbed by the neutral IGM.

As noted earlier, as the fireball expands and cools, its spectral peak steadily advances to longer wavelengths. This is manifest in the signal in the four NIR channels in the left panel of Figure 12. The signal peaks at later times at longer wavelengths as the temperature of the fireball falls with time. The luminosity persists for longer times at larger wavelengths because the shock emits at these energies for a larger fraction of its cooling

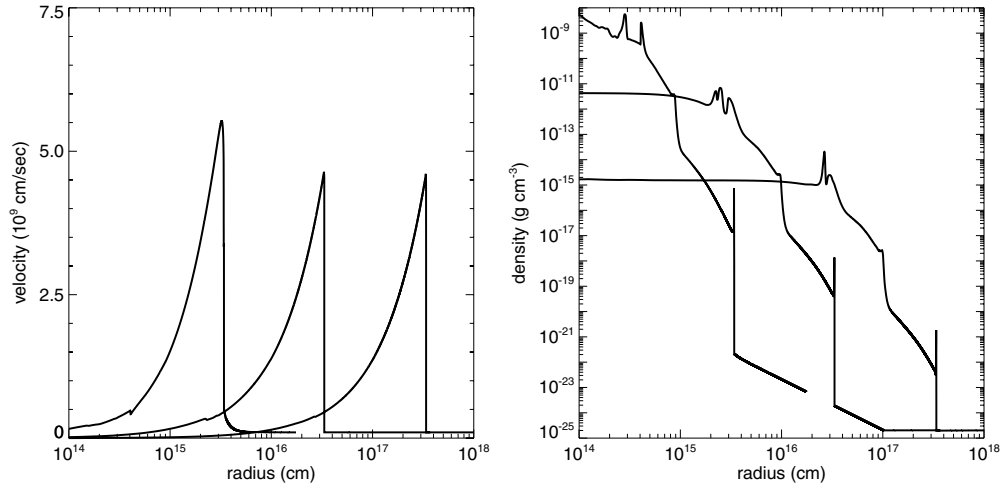


Figure 9. Intermediate to late-time hydrodynamical evolution of the u250 PI SN. Left panel: velocities at 8.36×10^5 s, 7.41×10^6 s, and 7.36×10^7 s (left to right). Right panel: density profiles at the same times from left to right.

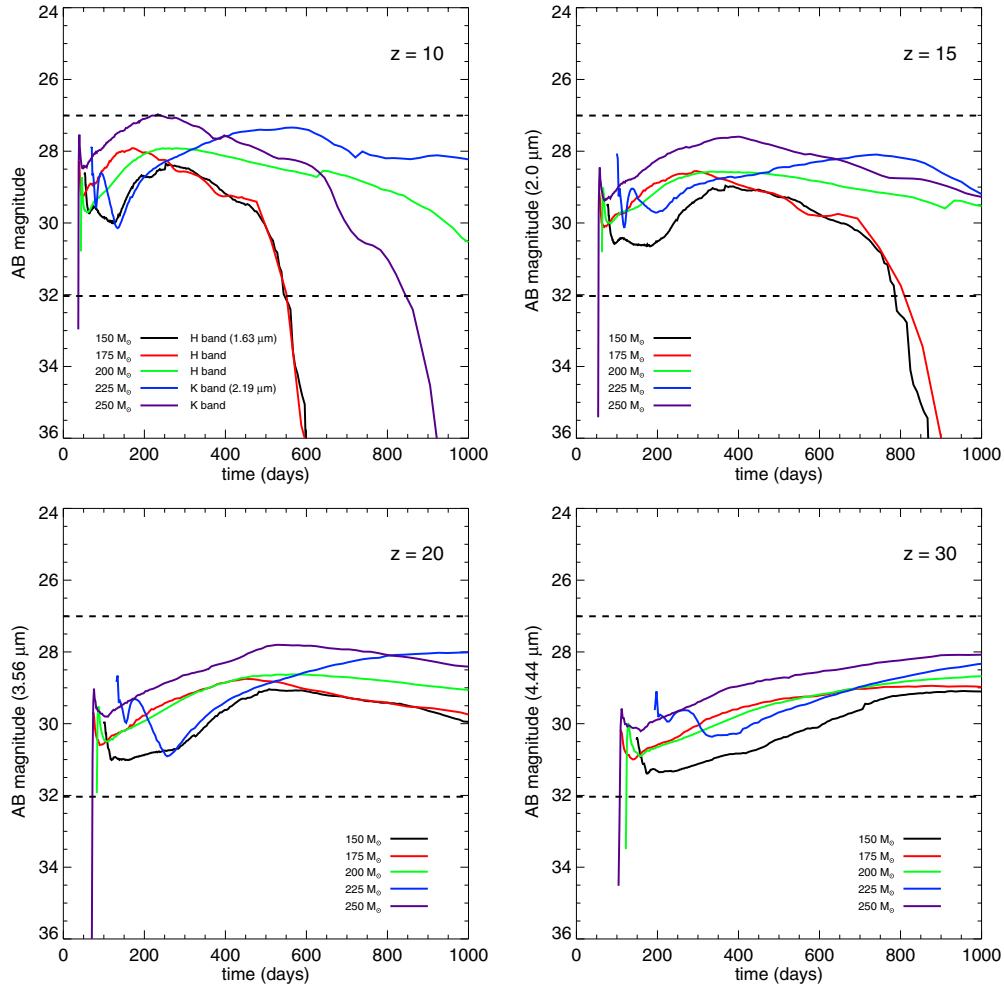


Figure 10. *JWST* NIRCcam light curves for the five u-series PI SNe. Redshifts ($z = 10, 15, 20, 30$) are noted in the upper right corner of each panel. The wavelength of the optimum *JWST* filter at each redshift is noted on the y-axis labels, and the times on the x-axes are in the observer frame. The dashed horizontal lines at AB mag 32 and 27 are *JWST* and WFIRST detection limits, respectively.

(A color version of this figure is available in the online journal.)

time than at higher energies. The expansion and cooling of the explosion, together with cosmological redshifting, also account for the shift of the NIR peak to later times and longer filter wavelengths with redshift in Figures 10 and 11. For example,

at $z = 10$ the u-series light curves peak from 200 to 600 days, and at $z = 30$ they peak after ~ 1000 days. As expected, the peak magnitude of each explosion rises with redshift. The *JWST* photometry and spectrometry limits are AB mag 31–32 and

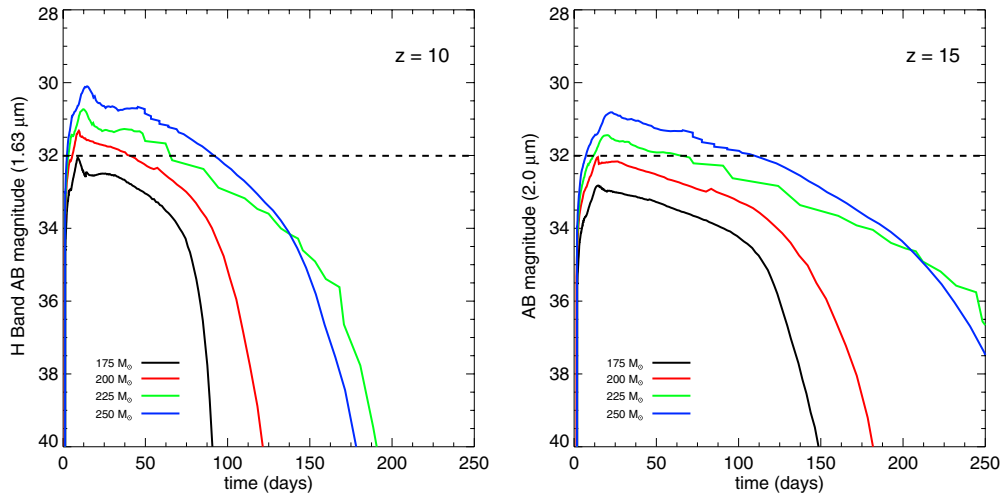


Figure 11. NIRCam light curves for the four z -series PI SNe. Left: $z = 10$. Right: $z = 15$.

(A color version of this figure is available in the online journal.)

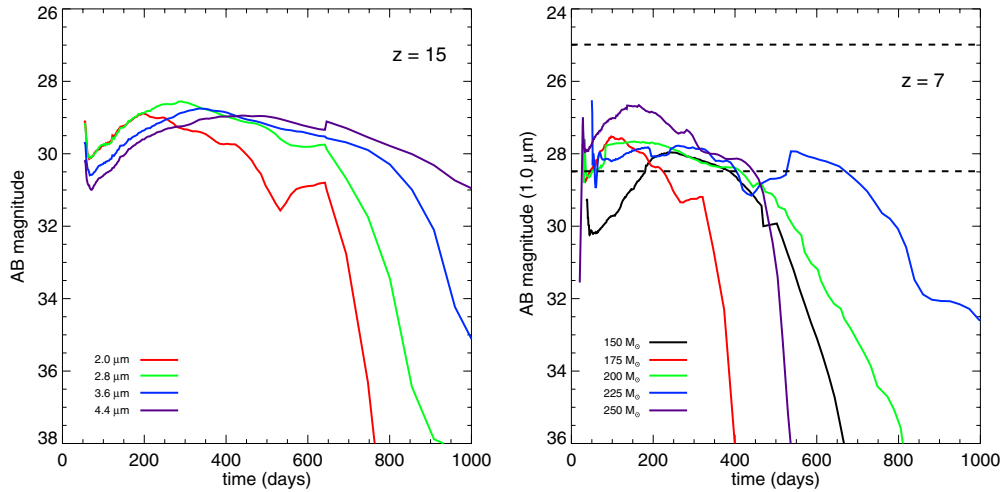


Figure 12. Left: spectral evolution of the u175 fireball in the NIR at $z = 10$. Right: Y -band ($1.0 \mu\text{m}$) light curves for all five u -series PI SNe at $z = 7$. The z -series explosions are too dim to be detected by LSST or Pan-STARRS at this redshift. The dashed horizontal lines at AB mag 28.5 and 25 are Pan-STARRS and LSST Y -band detection limits, respectively (these thresholds assume spectral stacking).

(A color version of this figure is available in the online journal.)

29–30, respectively. Spectrometry will be possible for all five u -series PI SNe at $z \gtrsim 30$ but for none of the z -series explosions at $z \gtrsim 10$. This is of note because resolving the order in which lines appear in spectra over time could provide a powerful probe of how heavy elements are mixed in the ejecta and thus of the explosion engine itself.

As noted in Whalen et al. (2013b), the NIR flux evolves on timescales of ~ 1000 days in the u -series and exhibits much more variability than the bolometric flux in the observer frame (which evolves over 40–90 yr) because of the expansion and cooling of the fireball. Such variability is the key to discriminating these events from primitive galaxies, with which they otherwise overlap in color-color space. Their NIR flux rises much more quickly than it falls, so it is easiest to detect them in their earliest stages, but they exhibit enough variation over survey times of one to five years to be identified at later stages as well. If Pop III PI SNe are found in the NIR, they will be thousands of times brighter than the halo or primitive galaxy that hosts them. Indeed, if a $z \sim 15$ object exhibited any variation in luminosity in a survey, in all likelihood it would be a PI SN in a primeval galaxy.

5.2. WFIRST, Euclid and WISH

Pop III PI SNe could be found in large numbers in future all-sky NIR surveys such as Euclid, WFIRST, and the Wide-field Imaging Surveyor for High-Redshift (WISH), whose target sensitivities at $2 \mu\text{m}$ are AB magnitudes 24, 27, and 27, respectively. Spectrum stacking is likely to extend the NIR detection limits of WFIRST and WISH to \sim AB mag 29. If so, it is clear from Figure 10 that WFIRST and WISH would detect u -series explosions out to $z \sim 15$ –20. Our calculations indicate that even at $z = 7$, all nine PI SNe will be above magnitude 25, so Euclid will only detect them below this redshift (although higher z might be possible with spectrum stacking). It may be that the optimal redshift range for locating Pop III PI SNe is $z \sim 15$ –20 because of Lyman-Werner (LW) UV feedback. LW backgrounds from the first stars are thought to destroy H_2 molecules and suppress cooling in primordial halos, causing them to grow more massive before their interiors can self-shield from LW photons, form H_2 , and host primordial star formation. Detailed numerical simulations show that the larger virial temperatures at the centers of such halos elevate cooling rates per H_2 molecule there by

two orders of magnitude, leading to higher central collapse rates that favor the formation of very massive stars (O’Shea & Norman 2007; Wise & Abel 2008b). LW backgrounds sufficient to postpone Pop III star formation likely did not arise until $z \sim 20$, delaying baryon cooling and collapse in halos until $z \sim 15$ –20. Global feedback may therefore enhance Pop III PI SN rates at slightly lower redshifts that are well within the range of WFIRST and WISH.

5.3. LSST/Pan-STARRS

Could high- z PI SNe be detected in all-sky optical and NIR surveys by the Large Synoptic Survey Telescope (LSST) or the Panoramic Survey Telescope & Rapid Response System (Pan-STARRS)? Unfortunately, above $z \sim 10$ source-frame wavelengths that would be redshifted into the optical are extinguished by Lyman absorption. But LSST will have a Y -band (0.95–1.070 μm) limit of AB magnitude 22 that may be extended to 25 with spectrum stacking. Pan-STARRS has a Y -band detection limit of AB magnitude 26 that can be extended above 28 by spectrum stacking. As shown in the right panel of Figure 12, the five u -series explosions will be visible to Pan-STARRS at $z = 7$ but not to LSST. As we discuss in greater detail below, it has been speculated that very massive Pop III stars could form down to $z \sim 6$ in pockets of metal-free gas; if so, their SNe could be detected by Pan-STARRS.

6. POP III PI SN DETECTION RATES

Although *JWST* will clearly be sensitive enough to detect $z \gtrsim 30$ PI SNe, will it encounter such explosions over reasonable survey times given its narrow field of view? Their detection in a given survey critically depends on their event rates, which in turn are governed by primordial star formation rates (SFRs) and the Pop III IMF. Many physical processes regulate the Pop III SFR over cosmic time. Metals and UV feedback from early generations of stars are especially important, since Pop III stars can only form in pristine gas and LW photons can destroy the H_2 required for baryons in halos to cool and collapse into stars (e.g., Haiman et al. 1997; Glover & Brand 2001; Machacek et al. 2001; Wise & Abel 2007; O’Shea & Norman 2008).

6.1. Semi-Analytical Estimates

The original estimates of Pop III PI SN rates were based on simple halo mass distributions and cosmological parameters that lead to first star formation at earlier epochs than do more improved parameters today (e.g., Komatsu et al. 2011). They predict event rates that range from 0.1 to $1.5 \text{ deg}^{-2} \text{ yr}^{-1}$ at $z \sim 25$ (Wise & Abel 2005; Weinmann & Lilly 2005) to 0.2 and $4 \text{ deg}^{-2} \text{ yr}^{-1}$ at $z \sim 25$ and 15, respectively (Weinmann & Lilly 2005). These rates exclude clustering and radiative and mechanical feedback between halos (e.g., O’Shea et al. 2005; Mesinger et al. 2006; MacIntyre et al. 2006; Whalen et al. 2008a, 2010) but do consider global LW UV backgrounds that can delay star formation to slightly later epochs.

6.2. Numerical Simulations

Cosmological simulations that incorporate chemical and radiative feedback in varying degrees of detail have produced more realistic Pop III SFRs for the first billion years of cosmic evolution (e.g., Tornatore et al. 2007; Trenti et al. 2009; Greif et al. 2010; Maio et al. 2011; Hummel et al. 2012; Johnson et al. 2013a; Wise et al. 2012). They basically agree on event rates at

high redshifts but differ somewhat from the original analytical estimates, mostly because they use more recent cosmological parameters. By modeling the rise of LW backgrounds and taking a simple approach to early metal enrichment, Hummel et al. (2012) find a cumulative rate of ~ 0.5 – $5 \text{ deg}^{-2} \text{ yr}^{-1}$ for Pop III PI SNe at $z \gtrsim 5$. Johnson et al. (2013a) find PI SN rates of $\sim 0.3 \text{ deg}^{-2} \text{ yr}^{-1}$ over the same redshift range, which are slightly lower because their models employ more sophisticated prescriptions for chemical and mechanical feedback by SNe and assume a less top-heavy Pop III IMF. They adopted a PI SN progenitor mass range of 140–260 M_\odot (e.g., Heger & Woosley 2002), but new models have since extended this range down to $\sim 65 M_\odot$ (Chatzopoulos & Wheeler 2012). This new lower limit revises the PI SN rate in Johnson et al. (2013a) upward by a factor of a few because of their choice of a Salpeter-like slope for the IMF.

6.3. $z = 15$ –20 and $\gtrsim 25$

The cumulative PI SN rates reported by Hummel et al. (2012) imply 10^{-3} – 10^{-2} events per yr per *JWST* NIRC2 field of view (10 arcmin^2). Thus, *JWST* should be able to find 5–10 PI SNe over the lifetime of the mission, but greater numbers may be found if more time is dedicated to the surveys. We note that Lyman absorption above $z \sim 6$, which we include in our study, may slightly reduce the detection rates predicted by Hummel et al. (2012). All-sky surveys will find far greater numbers of PI SNe, albeit at somewhat lower redshifts. Given the PI SN rates reported by Hummel et al. (2012) and Johnson et al. (2013a), up to $\sim 10^3$ PI SNe per yr could be found at $15 < z < 20$ by WFIRST and WISH.

6.4. $z \lesssim 10$

As noted earlier, PI SNe may also be found in all-sky optical and NIR surveys by LSST or Pan-STARRS but at lower redshifts ($z \lesssim 10$) because of extinction by Lyman absorption (see also Frost et al. 2009, for a recent PI SN detection campaign in *Spitzer* data). Thus, if very massive Pop III stars form at $6 \lesssim z \lesssim 10$, these surveys may discover their SNe if their rates are sufficiently high. Several recent numerical simulations suggest that such stars could form in isolated pockets of metal-free gas at $z \lesssim 6$ (Tornatore et al. 2007; Trenti & Stiavelli 2009; Trenti et al. 2009), and such environments have now been discovered at even lower redshifts (Fumagalli et al. 2011). Including LW backgrounds and a simple prescription for metal enrichment based on a numerical simulation, Trenti et al. (2009) estimate a cumulative Pop III PI SN rate of $\sim 10^{-2} \text{ yr}^{-1} \text{ deg}^{-2}$ at $5 \lesssim z \lesssim 10$, which implies an all-sky rate of up to $\sim 10^3 \text{ yr}^{-1}$.

Other cosmological simulations that include chemical enrichment and mechanical feedback by SNe have found lower Pop III SFRs (e.g., Tornatore et al. 2007; Maio et al. 2011) that imply PI SN rates that are smaller than Trenti et al. (2009). However, newer models with better treatments of LW feedback and chemical enrichment now suggest that PI SN rates in this redshift range are higher by roughly an order of magnitude than those of Tornatore et al. (2007) and Maio et al. (2011; Hummel et al. 2012; Johnson et al. 2013a). Since the Pop III SFR down to $z \sim 7$ reported by Wise et al. (2012) is in good agreement with that found by Johnson et al. (2013a), their results are also consistent with a high PI SN rate.¹⁴ Overall, the results of numerical simulations indicate that the all-sky Pop III PI SN rate at

¹⁴ See also Ahn et al. (2012), who find a similar evolution of the LW background due to massive Pop III stars at high z .

$6 \lesssim z \lesssim 10$ may lie between $\sim 10^3$ and 10^4 yr^{-1} , which bodes well for their detection by LSST and Pan-STARRS.

7. CONCLUSION

We find that Pop III PI SNe will be visible in deep field surveys by *JWST* out to $z \gtrsim 30$ and in all-sky surveys by WFIRST out to $z \sim 15\text{--}20$. They occur at rates that are sufficient to appear in deep field searches but will be discovered in much greater numbers in all-sky surveys that can be followed up by *JWST* and ground-based instruments. It may also be possible to find PI SNe at lower redshifts in current surveys, for example, as Lyman break dropouts in the *Hubble Space Telescope* (HST) CANDELS survey or with the new Subaru Hyper Suprime Cam. Such strategies will be the focus of future studies.

Our calculations emphasize the detection of Pop III PI SNe in the first few years of the explosion, but could their remnants be detected at later times by different means? Whalen et al. (2008c) found that PI SNe in ionized halos eventually emit up to half of the original energy of the explosion as H and He lines as the remnant sweeps up and shocks the relic H II region. Unfortunately, the luminosity of these lines is too low and redshifted to be directly detected. However, PI SNe can also deposit up to half of their energy into cosmic microwave background (CMB) photons by inverse Compton scattering and could impose excess power on the CMB at small scales (Oh et al. 2003; Kitayama & Yoshida 2005; Whalen et al. 2008c). The resolution of current ground-based CMB telescopes such as the Atacama Cosmology Telescope and South Pole Telescope approaches that required to directly image Sunyaev–Zeldovich fluctuations from individual Pop III PI SN remnants, so future observatories may detect them.

The extreme NIR luminosities of primordial PI SNe could contribute to an NIR background excess, as has been suggested for Pop III stars themselves (i.e., Kashlinsky et al. 2005). X-rays from gas plowed up by PI SN remnants, together with radiation from early black holes, would also build up an X-ray background at high redshifts. Indeed, Johnson & Khochfar (2011) have determined that X-rays from Pop III SN remnants may have accounted for $\sim 10\%$ of the reionizing photon budget at early times. New calculations show that PI SNe will probably not appear at 21 cm because of their lower event rates at high redshift and because their remnants will not emit enough synchrotron radiation to be directly detected by existing or future 21 cm observatories (Meiksin & Whalen 2013). The imprint of Pop III PI SNe on the CMB and NIR backgrounds will be addressed in future studies.

If, as some numerical simulations and stellar archaeology suggest, gas in primordial halos fragmented into multiple Pop III stars that were tens of solar masses instead of hundreds, then CC SNe also occurred in the primeval universe. Such explosions would be similar in brightness to those in the local universe today because their central engines mostly depend on the structure of the inner $3\text{--}4 M_\odot$ of the star, which does not vary strongly with metallicity (Chieffi & Limongi 2004; Woosley & Heger 2007; Whalen & Fryer 2012). Because they are 100 times dimmer than PI SNe and have softer spectra, less of their luminosity survives Lyman absorption by the neutral IGM at high redshift. However, because a dozen or more such stars may form in the halo, CC SNe may be more plentiful than PI SNe, which would enhance their likelihood of detection. Furthermore, if the star ejects a massive shell before exploding, the SN ejecta will light up the shell in the UV upon crashing into it (superluminous Type IIn SNe; Smith & McCray 2007; van Marle et al. 2010). Such

events can have luminosities that can rival those of PI SNe, and they might be visible at higher redshifts than Type II explosions (Moriya et al. 2010; Tanaka et al. 2012; Moriya et al. 2013). A new class of supermassive Pop III PI SNe has also now been discovered in numerical simulations that may be associated with the births of SMBH seeds (Montero et al. 2012; A. Heger & K. J. Chen 2013, in preparation; Johnson et al. 2013b; Whalen et al. 2013d, 2013e). We have calculated light curves and spectra for all three kinds of explosions and found that they can be seen at $z \sim 15\text{--}20$ by both *JWST* and WFIRST (Whalen et al. 2012, 2013a, 2013c; see also Tominaga et al. 2011).

A few Pop III stars may die in gamma-ray bursts (GRBs; e.g., Bromm & Loeb 2006; Wang et al. 2012), driven by either the collapse of very massive rapidly rotating stars (Suwa & Ioka 2011; Nagakura et al. 2012) or binary mergers with other $20\text{--}50 M_\odot$ stars (e.g., Fryer & Woosley 1998; Fryer et al. 1999, 2007; Zhang & Fryer 2001). This is corroborated by the fact that a fraction of Pop III stars have been found to form in binaries in simulations (Turk et al. 2009). Although X-rays from these events can trigger *Swift* or its successors such as the Joint Astrophysics Nascent Universe Satellite (JANUS, Mészáros & Rees 2010; Roming 2008; Burrows et al. 2010), their afterglows (Whalen et al. 2008b) are more likely to be detected in all-sky radio surveys by the Extended Very-Large Array, eMERLIN, and the Square Kilometer Array (de Souza et al. 2011b) due to their low event rates. We are now evaluating detection limits for Pop III GRBs in a variety of circumstellar environments (Mesler et al. 2012, R. A. Mesler et al. 2013, in preparation).

Finally, strong gravitational lensing by massive intervening galaxies and clusters at $z \sim 0\text{--}1$ could boost flux from Pop III SNe, more than compensating for Lyman absorption and improving prospects for their detection (Rydberg et al. 2013). The probability that flux from a Pop III SN would be lensed in an all-sky survey and the degree of magnification both depend on the event rate at the given redshift and may be fairly low. We have performed preliminary calculations that place the likelihood of lensing of $z \sim 20$ objects at $\sim 1\%\text{--}5\%$ for flux boosts of 2–5. Much higher boosts (10–300) are possible near the edges of massive clusters but with much smaller search volumes and lower probabilities of encountering high- z SNe. We are now developing and refining Markov Chain Monte Carlo ray-tracing models of strong gravitational lensing of $z \sim 20$ events, the highest redshifts ever attempted, in order to assess its potential to reveal primeval SNe and galaxies. Although strong lensing is not necessary for detecting PI SNe, it may be key to finding CC SNe in protogalaxies prior to reionization, less of whose flux survives Lyman absorption but whose higher event rates may favor the magnification of this flux.

The detection of primordial SNe will directly probe the Pop III IMF for the first time and reveal the environments in which they form. Their event rates will also trace the evolution of the first stellar populations. Pop III PI SN explosions at $z \sim 10\text{--}15$ will mark the positions of primeval galaxies on the sky that might not otherwise be found by *JWST* or TMT. Their discovery will open a direct window on the era of first light.

We thank the anonymous referee, whose comments improved the quality of this paper. D.J.W. is grateful for helpful discussions with Edo Berger, Ranga Ram Chary, Daniel Kasen, Avi Loeb, Pete Roming, and the many participants at First Stars and Galaxies: Challenges for the Next Decade, held at UT Austin March 8–11, 2010. He also acknowledges support from the Bruce and Astrid McWilliams Center for Cosmology at

Carnegie Mellon University and from the Baden-Württemberg-Stiftung by contract research via the programme Internationale Spitzenforschung II (grant P-LS-SPII/18). J.L.J. was supported by an LANL LDRD Director's Fellowship. M.S. thanks Marcia Rieke for making the NIRCcam filter curves available and was partially supported by NASA JWST grant NAG5-12458. D.E.H. was supported from the National Science Foundation CAREER grant PHY-1151836. A.H. was supported by the U.S. Department of Energy under contracts DE-FC02-01ER41176, FC02-09ER41618 (SciDAC), and DE-FG02-87ER40328. S.E.W. was supported by the National Science Foundation grant AST-0909129 and the NASA Theory Program grant NNX09AK36G. Work at LANL was done under the auspices of the National Nuclear Security Administration of the U.S. Department of Energy at Los Alamos National Laboratory under Contract No. DE-AC52-06NA25396. All RAGE and SPECTRUM calculations were performed on Institutional Computing (IC) and Yellow network platforms at LANL (Mustang, Pinto, Conejo, Lobo, and Yellowrail).

REFERENCES

- Abel, T., Bryan, G. L., & Norman, M. L. 2000, *ApJ*, **540**, 39
- Abel, T., Bryan, G. L., & Norman, M. L. 2002, *Sci*, **295**, 93
- Abel, T., Wise, J. H., & Bryan, G. L. 2007, *ApJL*, **659**, L87
- Agarwal, B., Khochfar, S., Johnson, J. L., et al. 2012, *MNRAS*, **425**, 2854
- Ahn, K., Iliev, I. T., Shapiro, P. R., et al. 2012, *ApJL*, **756**, L16
- Alvarez, M. A., Bromm, V., & Shapiro, P. R. 2006, *ApJ*, **639**, 621
- Alvarez, M. A., Wise, J. H., & Abel, T. 2009, *ApJL*, **701**, L133
- Baraffe, I., Heger, A., & Woosley, S. E. 2001, *ApJ*, **550**, 890
- Barkat, Z., Rakavy, G., & Sack, N. 1967, *PhRvL*, **18**, 379
- Beers, T. C., & Christlieb, N. 2005, *ARA&A*, **43**, 531
- Blinnikov, S., Lundqvist, P., Bartunov, O., Nomoto, K., & Iwamoto, K. 2000, *ApJ*, **532**, 1132
- Blinnikov, S. I., & Tolstov, A. G. 2011, *AstL*, **37**, 194
- Bromm, V., Coppi, P. S., & Larson, R. B. 1999, *ApJL*, **527**, L5
- Bromm, V., Coppi, P. S., & Larson, R. B. 2002, *ApJ*, **564**, 23
- Bromm, V., Ferrara, A., Coppi, P. S., & Larson, R. B. 2001, *MNRAS*, **328**, 969
- Bromm, V., & Loeb, A. 2003, *ApJ*, **596**, 34
- Bromm, V., & Loeb, A. 2006, *ApJ*, **642**, 382
- Bromm, V., Yoshida, N., & Hernquist, L. 2003, *ApJL*, **596**, L135
- Burrows, D. N., Roming, P. W. A., Fox, D. B., et al. 2010, *Proc. SPIE*, **7732**
- Caffau, E., Bonifacio, P., François, P., et al. 2012, *A&A*, **542**, A51
- Cayrel, R., Depagne, E., Spite, M., et al. 2004, *A&A*, **416**, 1117
- Chatzopoulos, E., & Wheeler, J. C. 2012, *ApJ*, **748**, 42
- Chen, K.-J., Heger, A., & Almgren, A. S. 2011, *CoPhC*, **182**, 254
- Chiaki, G., Yoshida, N., & Kitayama, T. 2013, *ApJ*, **762**, 50
- Chieffi, A., & Limongi, M. 2004, *ApJ*, **608**, 405
- Choi, J.-H., Shlosman, I., & Begelman, M. C. 2013, *ApJ*, **774**, 149
- Clark, P. C., Glover, S. C. O., Smith, R. J., et al. 2011, *Sci*, **331**, 1040
- Colgate, S. A. 1974, *ApJ*, **187**, 333
- Cooke, R., Pettini, M., Steidel, C. C., Rudie, G. C., & Jorgenson, R. A. 2011, *MNRAS*, **412**, 1047
- Crowther, P. A., Schnurr, O., Hirschi, R., et al. 2010, *MNRAS*, **408**, 731
- de Souza, R. S., Ishida, E. E. O., Johnson, J. L., Whalen, D. J., & Mesinger, A. 2013, arXiv:1306.4984
- de Souza, R. S., Rodrigues, L. F. S., Ishida, E. E. O., & Opher, R. 2011a, *MNRAS*, **415**, 2969
- de Souza, R. S., Yoshida, N., & Ioka, K. 2011b, *A&A*, **533**, A32
- Dessart, L., Hillier, D. J., Waldman, R., Livne, E., & Blondin, S. 2012, *MNRAS*, **426**, L76
- Dessart, L., Waldman, R., Livne, E., Hillier, D. J., & Blondin, S. 2013, *MNRAS*, **428**, 3227
- Djorgovski, S. G., Volonteri, M., Springel, V., Bromm, V., & Meylan, G. 2008, in *The Eleventh Marcel Grossmann Meeting on Recent Developments in Theoretical and Experimental General Relativity, Gravitation and Relativistic Field Theories*, ed. H. Kleinert, R. T. Jantzen, & R. Ruffini (Singapore: World Scientific Publishing), **340**
- Dwek, E., & Arendt, R. G. 2008, *ApJ*, **685**, 976
- Ekström, S., Meynet, G., Chiappini, C., Hirschi, R., & Maeder, A. 2008, *A&A*, **489**, 685
- Ensmann, L., & Burrows, A. 1992, *ApJ*, **393**, 742
- Frebel, A., Aoki, W., Christlieb, N., et al. 2005, *Natur*, **434**, 871
- Frey, L. H., Even, W., Whalen, D. J., et al. 2013, *ApJS*, **204**, 16
- Frost, M. I., Surace, J., Moustakas, L. A., & Krick, J. 2009, *ApJL*, **698**, L68
- Fryer, C. L., Mazzali, P. A., Prochaska, J., et al. 2007, *PASP*, **119**, 1211
- Fryer, C. L., Whalen, D. J., & Frey, L. 2010, in *AIP Conf. Ser.* 1294, *The First Stars and Galaxies: Challenges for the Next Decade*, ed. D. J. Whalen, V. Bromm, & N. Yoshida (Melville: NY: AIP), **70**
- Fryer, C. L., & Woosley, S. E. 1998, *ApJL*, **502**, L9
- Fryer, C. L., Woosley, S. E., & Hartmann, D. H. 1999, *ApJ*, **526**, 152
- Fumagalli, M., O'Meara, J. M., & Prochaska, J. X. 2011, *Sci*, **334**, 1245
- Gal-Yam, A., Mazzali, P., Ofek, E. O., et al. 2009, *Natur*, **462**, 624
- Gardner, J. P., Mather, J. C., Clampin, M., et al. 2006, *SSRv*, **123**, 485
- Gezari, S., Dessart, L., Basa, S., et al. 2008, *ApJL*, **683**, L131
- Gittings, M., Weaver, R., Clover, M., et al. 2008, *CS&D*, **1**, 015005
- Glover, S. 2013, in *The First Galaxies*, ed. T. Wiklund, B. Mobasher, & V. Bromm (Astrophysics and Space Science Library, Vol. 396; Berlin: Springer), **103**
- Glover, S. C. O., & Brand, P. W. J. L. 2001, *MNRAS*, **321**, 385
- Greif, T. H., Bromm, V., Clark, P. C., et al. 2012, *MNRAS*, **424**, 399
- Greif, T. H., Glover, S. C. O., Bromm, V., & Klessen, R. S. 2010, *ApJ*, **716**, 510
- Greif, T. H., Johnson, J. L., Bromm, V., & Klessen, R. S. 2007, *ApJ*, **670**, 1
- Greif, T. H., Johnson, J. L., Klessen, R. S., & Bromm, V. 2008, *MNRAS*, **387**, 1021
- Greif, T. H., Springel, V., White, S. D. M., et al. 2011, *ApJ*, **737**, 75
- Haiman, Z., Rees, M. J., & Loeb, A. 1997, *ApJ*, **476**, 458
- Heger, A., & Woosley, S. E. 2002, *ApJ*, **567**, 532
- Hirano, S., Hosokawa, T., Yoshida, N., et al. 2013, arXiv:1308.4456
- Hosokawa, T., Omukai, K., Yoshida, N., & Yorke, H. W. 2011, *Sci*, **334**, 1250
- Hosokawa, T., Yoshida, N., Omukai, K., & Yorke, H. W. 2012, *ApJL*, **760**, L37
- Hummel, J. A., Pawlik, A. H., Milosavljević, M., & Bromm, V. 2012, *ApJ*, **755**, 72
- Iglesias, C. A., & Rogers, F. J. 1996, *ApJ*, **464**, 943
- Jeon, M., Pawlik, A. H., Greif, T. H., et al. 2012, *ApJ*, **754**, 34
- Joggerst, C. C., Almgren, A., Bell, J., et al. 2010, *ApJ*, **709**, 11
- Joggerst, C. C., & Whalen, D. J. 2011, *ApJ*, **728**, 129
- Johnson, J. L., & Bromm, V. 2007, *MNRAS*, **374**, 1557
- Johnson, J. L., Dalla, V. C., & Khochfar, S. 2013a, *MNRAS*, **428**, 1857
- Johnson, J. L., Greif, T. H., & Bromm, V. 2008, *MNRAS*, **388**, 26
- Johnson, J. L., Greif, T. H., Bromm, V., Klessen, R. S., & Ippolito, J. 2009, *MNRAS*, **399**, 37
- Johnson, J. L., & Khochfar, S. 2011, *ApJ*, **743**, 126
- Johnson, J. L., Whalen, D. J., Even, W., et al. 2013b, *ApJ*, **775**, 107
- Johnson, J. L., Whalen, D. J., Fryer, C. L., & Li, H. 2012, *ApJ*, **750**, 66
- Johnson, J. L., Whalen, D. J., Li, H., & Holz, D. E. 2013c, *ApJ*, **771**, 116
- Karlsson, T., Johnson, J. L., & Bromm, V. 2008, *ApJ*, **679**, 6
- Kasen, D., & Bildsten, L. 2010, *ApJ*, **717**, 245
- Kasen, D., Woosley, S. E., & Heger, A. 2011, *ApJ*, **734**, 102
- Kashlinsky, A., Arendt, R. G., Mather, J., & Moseley, S. H. 2005, *Natur*, **438**, 45
- Katz, B., Sapir, N., & Waxman, E. 2012, *ApJ*, **747**, 147
- Kitayama, T., & Yoshida, N. 2005, *ApJ*, **630**, 675
- Kitayama, T., Yoshida, N., Susa, H., & Umemura, M. 2004, *ApJ*, **613**, 631
- Komatsu, E., Smith, K. M., Dunkley, J., et al. 2011, *ApJS*, **192**, 18
- Krtićka, J., & Kubát, J. 2006, *A&A*, **446**, 1039
- Kudritzki, R. 2000, in *The First Stars*, ed. A. Weiss, T. G. Abel, & V. Hill (Berlin: Springer), **127**
- Lai, D. K., Bolte, M., Johnson, J. A., et al. 2008, *ApJ*, **681**, 1524
- Latif, M. A., Schleicher, D. R. G., Schmidt, W., & Niemeyer, J. 2013a, *MNRAS*, **433**, 1607
- Latif, M. A., Schleicher, D. R. G., Schmidt, W., & Niemeyer, J. 2013b, *MNRAS*, **430**, 588
- Lippai, Z., Frei, Z., & Haiman, Z. 2009, *ApJ*, **701**, 360
- Machacek, M. E., Bryan, G. L., & Abel, T. 2001, *ApJ*, **548**, 509
- MacIntyre, M. A., Santoro, F., & Thomas, P. A. 2006, *MNRAS*, **368**, 1301
- Mackey, J., Bromm, V., & Hernquist, L. 2003, *ApJ*, **586**, 1
- Madau, P. 1995, *ApJ*, **441**, 18
- Magee, N. H., Abdallah, J., Jr., Clark, R. E. H., et al. 1995, in *ASP Conf. Ser.* 78, *Astrophysical Applications of Powerful New Databases*, ed. S. J. Adelman & W. L. Wiese (San Francisco, CA: ASP), **51**
- Maio, U., Khochfar, S., Johnson, J. L., & Ciardi, B. 2011, *MNRAS*, **414**, 1145
- Matzner, C. D., & McKee, C. F. 1999, *ApJ*, **510**, 379
- McKee, C. F., & Tan, J. C. 2008, *ApJ*, **681**, 771
- Meiksin, A., & Whalen, D. J. 2013, *MNRAS*, **430**, 2854
- Mesinger, A., Johnson, B. D., & Haiman, Z. 2006, *ApJ*, **637**, 80
- Mesler, R. A., Whalen, D. J., Lloyd-Ronning, N. M., Fryer, C. L., & Pihlström, Y. M. 2012, *ApJ*, **757**, 117
- Mészáros, P., & Rees, M. J. 2010, *ApJ*, **715**, 967

- Meynet, G., Maeder, A., Schaller, G., Schaerer, D., & Charbonnel, C. 1994, *A&AS*, **103**, 97
- Milosavljević, M., Bromm, V., Couch, S. M., & Oh, S. P. 2009, *ApJ*, **698**, 766
- Montero, P. J., Janka, H.-T., & Müller, E. 2012, *ApJ*, **749**, 37
- Moriya, T., Yoshida, N., Tominaga, N., et al. 2010, in AIP Conf. Ser. 1294, The First Stars and Galaxies: Challenges for the Next Decade, ed. D. J. Whalen, V. Bromm, & N. Yoshida (Melville, NY: AIP), 268
- Moriya, T. J., Blinnikov, S. I., Tominaga, N., et al. 2013, *MNRAS*, **428**, 1020
- Nagakura, H., Suwa, Y., & Ioka, K. 2012, *ApJ*, **754**, 85
- Nakamura, F., & Umemura, M. 2001, *ApJ*, **548**, 19
- Nakar, E., & Sari, R. 2010, *ApJ*, **725**, 904
- Oh, S. P., Cooray, A., & Kamionkowski, M. 2003, *MNRAS*, **342**, L20
- Omukai, K., & Inutsuka, S.-i. 2002, *MNRAS*, **332**, 59
- Omukai, K., & Palla, F. 2001, *ApJL*, **561**, L55
- Omukai, K., & Palla, F. 2003, *ApJ*, **589**, 677
- O'Shea, B. W., Abel, T., Whalen, D., & Norman, M. L. 2005, *ApJL*, **628**, L5
- O'Shea, B. W., & Norman, M. L. 2007, *ApJ*, **654**, 66
- O'Shea, B. W., & Norman, M. L. 2008, *ApJ*, **673**, 14
- Pan, T., Kasen, D., & Loeb, A. 2012a, *MNRAS*, **422**, 2701
- Pan, T., Loeb, A., & Kasen, D. 2012b, *MNRAS*, **423**, 2203
- Park, K., & Ricotti, M. 2011, *ApJ*, **739**, 2
- Park, K., & Ricotti, M. 2012, *ApJ*, **747**, 9
- Park, K., & Ricotti, M. 2013, *ApJ*, **767**, 163
- Pawlik, A. H., Milosavljević, M., & Bromm, V. 2011, *ApJ*, **731**, 54
- Pawlik, A. H., Milosavljević, M., & Bromm, V. 2013, *ApJ*, **767**, 59
- Piro, A. L., Chang, P., & Weinberg, N. N. 2010, *ApJ*, **708**, 598
- Rakavy, G., & Shaviv, G. 1967, *ApJ*, **148**, 803
- Ren, J., Christlieb, N., & Zhao, G. 2012, *RAA*, **12**, 1637
- Ritter, J. S., Safranek-Shrader, C., Gnat, O., Milosavljević, M., & Bromm, V. 2012, *ApJ*, **761**, 56
- Rogers, F. J., Swenson, F. J., & Iglesias, C. A. 1996, *ApJ*, **456**, 902
- Roming, P. 2008, in COSPAR, Plenary Meeting, Vol. 37, 37th COSPAR Scientific Assembly, 2645
- Rydberg, C.-E., Zackrisson, E., Lundqvist, P., & Scott, P. 2013, *MNRAS*, **429**, 3658
- Rydberg, C. E., Zackrisson, E., & Scott, P. 2010, in Cosmic Radiation Fields: Sources in the Early Universe (CRF 2010), ed. M. Raue, T. Kneiske, D. Horns, D. Elsaesser, & P. Hauschildt (Hamburg: DESY), 26
- Safranek-Shrader, C., Milosavljevic, M., & Bromm, V. 2013, arXiv:1307.1982
- Scannapieco, E., Madau, P., Woosley, S., Heger, A., & Ferrara, A. 2005, *ApJ*, **633**, 1031
- Schaerer, D. 2002, *A&A*, **382**, 28
- Schawinski, K., Justham, S., Wolf, C., et al. 2008, *Sci*, **321**, 223
- Schleicher, D. R. G., Palla, F., Ferrara, A., Galli, D., & Latif, M. 2013, *A&A*, **558A**, 59
- Schober, J., Schleicher, D., Federrath, C., et al. 2012, *ApJ*, **754**, 99
- Smith, B. D., & Sigurdsson, S. 2007, *ApJL*, **661**, L5
- Smith, B. D., Turk, M. J., Sigurdsson, S., O'Shea, B. W., & Norman, M. L. 2009, *ApJ*, **691**, 441
- Smith, N., & McCray, R. 2007, *ApJL*, **671**, L17
- Soderberg, A. M., Berger, E., Page, K. L., et al. 2008, *Natur*, **453**, 469
- Stacy, A., Bromm, V., & Loeb, A. 2011, *MNRAS*, **413**, 543
- Stacy, A., Greif, T. H., & Bromm, V. 2010, *MNRAS*, **403**, 45
- Stacy, A., Greif, T. H., & Bromm, V. 2012, *MNRAS*, **422**, 290
- Stacy, A., Greif, T. H., Klessen, R. S., Bromm, V., & Loeb, A. 2013, *MNRAS*, **431**, 1470
- Su, J., Stiavelli, M., Oesch, P., et al. 2011, *ApJ*, **738**, 123
- Susa, H. 2013, *ApJ*, **773**, 185
- Suwa, Y., & Ioka, K. 2011, *ApJ*, **726**, 107
- Tan, J. C., & McKee, C. F. 2004, *ApJ*, **603**, 383
- Tanaka, M., Moriya, T. J., Yoshida, N., & Nomoto, K. 2012, *MNRAS*, **422**, 2675
- Tanaka, T., & Haiman, Z. 2009, *ApJ*, **696**, 1798
- Tolstov, A. G. 2010, *AstL*, **36**, 109
- Tolstov, A. G., Blinnikov, S. I., & Nadyozhin, D. K. 2013, *MNRAS*, **429**, 3181
- Tominaga, N., Blinnikov, S., Baklanov, P., et al. 2009, *ApJL*, **705**, L10
- Tominaga, N., Morokuma, T., Blinnikov, S. I., et al. 2011, *ApJS*, **193**, 20
- Tornatore, L., Ferrara, A., & Schneider, R. 2007, *MNRAS*, **382**, 945
- Trenti, M., & Stiavelli, M. 2009, *ApJ*, **694**, 879
- Trenti, M., Stiavelli, M., & Michael Shull, J. 2009, *ApJ*, **700**, 1672
- Turk, M. J., Abel, T., & O'Shea, B. 2009, *Sci*, **325**, 601
- van Marle, A. J., Smith, N., Owocki, S. P., & van Veelen, B. 2010, *MNRAS*, **407**, 2305
- Vasiliev, E. O., Vorobyov, E. I., Matvienko, E. E., Razoumov, A. O., & Shchekinov, Y. A. 2012, *ARep*, **56**, 895
- Vink, J. S., de Koter, A., & Lamers, H. J. G. L. M. 2001, *A&A*, **369**, 574
- Wang, F. Y., Bromm, V., Greif, T. H., et al. 2012, *ApJ*, **760**, 27
- Weaver, T. A., Zimmerman, G. B., & Woosley, S. E. 1978, *ApJ*, **225**, 1021
- Weinmann, S. M., & Lilly, S. J. 2005, *ApJ*, **624**, 526
- Whalen, D., Abel, T., & Norman, M. L. 2004, *ApJ*, **610**, 14
- Whalen, D., Hueckstaedt, R. M., & McConkie, T. O. 2010, *ApJ*, **712**, 101
- Whalen, D., & Norman, M. L. 2006, *ApJS*, **162**, 281
- Whalen, D., & Norman, M. L. 2008a, *ApJ*, **673**, 664
- Whalen, D., O'Shea, B. W., Smidt, J., & Norman, M. L. 2008a, *ApJ*, **679**, 925
- Whalen, D., Prochaska, J. X., Heger, A., & Tumlinson, J. 2008b, *ApJ*, **682**, 1114
- Whalen, D., van Veelen, B., O'Shea, B. W., & Norman, M. L. 2008c, *ApJ*, **682**, 49
- Whalen, D. J. 2012, arXiv:1209.4688
- Whalen, D. J., Even, W., Lovekin, C. C., et al. 2013a, *ApJ*, **768**, 195
- Whalen, D. J., & Fryer, C. L. 2012, *ApJL*, **756**, L19
- Whalen, D. J., Fryer, C. L., Holz, D. E., et al. 2013b, *ApJL*, **762**, L6
- Whalen, D. J., Heger, A., Chen, K.-J., et al. 2012, arXiv:1211.1815
- Whalen, D. J., Joggerst, C. C., Fryer, C. L., et al. 2013c, *ApJ*, **768**, 95
- Whalen, D. J., Johnson, J. J., Smidt, J., et al. 2013d, *ApJ*, **774**, 64
- Whalen, D. J., Johnson, J. L., Smidt, J., et al. 2013e, arXiv:1308.3278
- Whalen, D. J., & Norman, M. L. 2008b, *ApJ*, **672**, 287
- Wise, J. H., & Abel, T. 2005, *ApJ*, **629**, 615
- Wise, J. H., & Abel, T. 2007, *ApJ*, **671**, 1559
- Wise, J. H., & Abel, T. 2008a, *ApJ*, **684**, 1
- Wise, J. H., & Abel, T. 2008b, *ApJ*, **685**, 40
- Wise, J. H., Turk, M. J., Norman, M. L., & Abel, T. 2012, *ApJ*, **745**, 50
- Woosley, S. E., & Heger, A. 2007, *PhR*, **442**, 269
- Woosley, S. E., Heger, A., & Weaver, T. A. 2002, *RvMP*, **74**, 1015
- Yoon, S.-C., Dierks, A., & Langer, N. 2012, *A&A*, **542**, A113
- Yoon, S.-C., Langer, N., & Norman, C. 2006, *A&A*, **460**, 199
- Yoshida, N., Omukai, K., & Hernquist, L. 2008, *Sci*, **321**, 669
- Young, D. R., Smartt, S. J., Valenti, S., et al. 2010, *A&A*, **512**, A70
- Zhang, W., & Fryer, C. L. 2001, *ApJ*, **550**, 357